Institut für Angewandte Photophysik

Fachrichtung Physik

Fakultät Mathematik und Naturwissenschaften

Technische Universität Dresden

Influence of Oxygen on laser induced Contamination

Diplomarbeit

zur Erlangung des akademischen Grades

Diplom-Physiker

vorgelegt von

Markus Hippler

geboren am 21. April 1990 in Torgau

Dresden 2015

**TECHNISCHE
UNIVERSITÄT
DRESDEN**

Eingereicht am 21.05.2015

1. Gutachter: Prof. Dr. phil. II. habil. Lukas M. Eng

2. Gutachter: Prof. Dr. rer. nat. Detlev Ristau

Danksagung

Kurzfassung

Bisherige Messmotheden ermöglichen keine ausreichend akkurate und insbesondere globale Vermessung von Windprofilen und deren Aerosolkonzentration. ESA's ADM-Aeolus Satellit soll dieser Herausforderung mit dem lidar Instrument Aladin (Atmospheric LAser Doppler INstrument) begegnen. Um atmosphärischen Rückstreumechanismen gerecht zu werden, wurde ein Lasersytem mit Frequenzverdreifachung auf 355 nm ausgewählt. Bedingt durch die Ausgasung organischer Moleküle kommt es beim Einsatz von sichtbarer und ultravioletter Strahlung in gekapselten Vakuumsystemen jedoch zu Kontaminationseffekten. Angesichts der erforderlichen hohen Pulsanzahl führt die sogenannte laserinduzierte Kontamination unweigerlich zum Systemausfall der Optik. In internationalen Kooperationen wurden bereits Präventionsmaßnahmen zur Vermeidung dieser Problematik in Form verbesserter Beschichtungen der Optiken untersucht. Diesbezüglich stellte sich die Anwesenheit von Sauerstoff ebenfalls als vielversprechend heraus. Das Ziel der vorliegenden Arbeit war dementsprechend die Quantifizierung des Einflusses von Sauerstoff auf die laserinduzierte Kontamination. Zur Prävention starker Kontaminationseffekte konnte mithilfe eines differentiell gepumpten Gasanalysators ein erforderlicher Schwellwert des Partialdruckes von Sauerstoff ermittelt werden. Die Gültigkeit des Sauerstoffschwellwertes wurde ferner an verschiedenen optischen Parametern gezeigt. Diese gewonnenen Erkenntnisse konnten von modellbasierten Kontaminanten auf reale Kontaminanten übertragen werden.

Contents

Abbreviations

ADM	Atmospheric Dynamic Mission
AFM	Atomic Force Microscope
AR	Anti Reflective
DIC	Differential Interference Contrast
E-Beam	Electron Beam Evaporation
EDX	Electron Dispersive X-ray spectroscopy
ESA	European Space Agency
FWHM	Full Width at Half Maximum
HR	High Reflective
IBS	Ion Beam Sputtering
ITP	Institute of Technical Physics
LIC	Laser Induced Contamination
LID	Laser Induced Damage
LIDT	Laser Induced Damage Threshold
LZH	Laserzentrum Hannover
MS	Magnetron Sputtering
PPM	Parts Per Million
RGA	Residual Gas Analyzer
ROI	Region Of Interest

SEM	Scanning Electron Microscope
SHG	Second Harmonic Generation
THG	Third Harmonic Generation
UV	Ultra Violett
WLIM	White Light Interference Microscope

1   Introduction

1.1   Motivation

Today it is impossible imaged without any kind of laser applications, especially in research and manufacturing topics. High sophisticated and powerful systems have a wide range of applications. Moreover, lasers are not only used in lab facilities anymore and gather more and more influence to orbital and space applications (e.g European Data Relay System [1] for inter satellite and geostationary communication and the LISA Pathfinder mission [2] concepted for the low frequency gravitational wave detection). European Space Agency (ESA) and its living planet program aims for novel earth observation methods from space based satellites. One of the programs subject is the Atmospheric Dynamic Mission (ADM)-Aeolus satellite. The purpose of ADM-Aeolus mission is the measurement of wind profiles from low earth orbital with high accuracy. To provide these information a lidar (Light Detection and Ranging) system is onboard. The principle of the lidar system is based on a laser system emitting high power pulses into the atmosphere. Vertical wind profiles are determined by the backscattered signal. The backscattered signal contains the information of the Doppler shift and the propagation time of the pulse.

Besides temperature, humidity and pressure it is necessary to have accurate wind profiles for global climate models. Current ground based instruments are limited in their coverage, whereas plane and balloon missions only provide local wind profiles. The ADM-Aeolus mission aims to fill this gap of information. Observing global wind profiles will be provided by the ADM-Aeolus for the first time ever.

The functionality of the space based Doppler wind lidar system is delivered

for the satellite by the instrument Aladin (Atmospheric LAser Doppler INstrument). It consists of a high power Nd:YAG laser emitting the light towards the atmosphere at an angle of 35° to nadir, orthogonal to the satellite's ground track velocity. Transmission and receiver telescope as well as an interferometry setup collects the backscattered signal and determines the time of flight as well as the frequency shift of the broadening. ADM-Aeolus is addressed to scan the global wind profiles of the planetary boundary layer(PBL), the troposphere and the lower stratosphere (0 - 30 km above sea level) every 12 hours at an altitude of 408 km. Thermal stability and sufficient solar panel illumination is ensured by a sun-synchronous dusk/dawn orbit. To reduce solar background noise, the laser is oriented to the night face of the earth. Figure 1.1 pictures its orbital and active measurement configuration. Minimum requirements of the
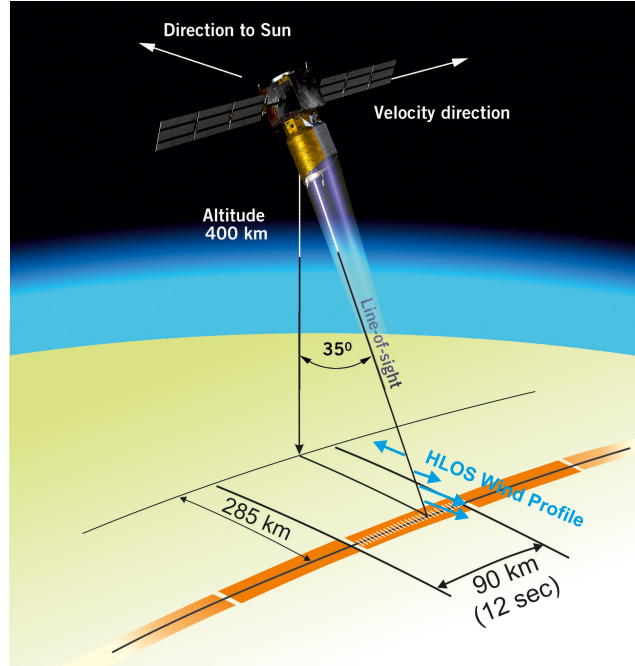
Figure 1.1: Illustrates ADM-Aeolus measurement geometry [3].

observation mission are listed in Table 1.1. This is necessary for a substantial improvement of current weather prediction and climate model simulations [3].

The fundamental wavelength of the pulsed Nd:YAG laser is 1064 nm. Considering scattering mechanisms of the atmosphere, a lower laser wavelength enables the measurement of aerosol concentrations simultaneously. This addi-

	PBL	Troposphere	Stratosphere
Vertical Domain [km]	0-2	2-16	16-30
Vertical Resolution [km]	0.5	1	2.5
Horizontal Domain		global	
Number of Profiles [hour^{-1}]		100	
Profile Separation [km]		200	
Temporal Sampling [hour]		12	
Accuracy [m s^{-1}]	2	2-3	3-5
Dynamic Range [m s^{-1}]		$\pm$ 150	
Horizontal Intergration [km]		50	

Table 1.1: Observational requirements on the ADM-Aeolus system during the
planned operation time of 3 years [3].

tional information is not yet considered in global climate models. Moreover,
the influence of the aerosol concentration on weather and climate phenomena is
not well known, especially not for global challenges. The scattering of the light
is characterized by the Mie scattering from aerosols and larger molecules and
by the Rayleigh-Brillouin scattering from atoms and small molecules. Light
with a comparable wavelength λ to the dimension d of aerosols or spheri-
cal molecules is elastically scattered and is described by the Mie scattering.
Whereas the Rayleigh-Brillouin scattering is described by elastic scattering at
molecules much smaller than the wavelength ($d << \lambda$), like oxygen or nitrogen.
The backscattered light will be effected by density fluctuations of the atmo-
sphere as well as broadened by the Brownian motion of the molecules. Con-
sider the fact, that the aerosol concentration decreases with the altitude and
the Rayleigh-Brillouin scattering will be the dominant scattering mechanism
at higher altitudes. Additionally, the cross section of the Rayleigh-Brillouin
scattering (see equation 1.1, with λ as the wavelength, n as the refractive index
and d as the particle size) depends highly on the wavelength λ [4]

$$\sigma_s = \frac{2\pi^5}{3} \frac{d^6}{\lambda^4} \left(\frac{n^2 - 1}{n^2 + 1} \right)^2 . \tag{1.1}$$

A short pulse is necessary to overcome the Rayleigh-Brillouin scattering in
higher altitudes and an ultraviolet (UV) wavelength is needed for the Mie
scattering. Moreover, UV pulses are in this case eye save. The fundamental

wavelength of the Nd:YAG laser will be tripled to a wavelength of 355 nm with second harmonic generation (SHG) conversion and followed by the sum frequency generation, the so called third harmonic generation (THG)[3].

Due to the different scattering mechanisms a high fluence of $1\,\mathrm{J/cm^2}$ and a short pulse duration of 30 ns will be used. The spectral width is 30 MHz and the laser will operate at a repetition rate of 80 Hz. The lasers configuration with its wavelength in the UV regime will face new challenges. Wavelengths in the visible and the UV spectra interacts highly with organic molecules and the organic molecules will be deposited on the optics surface, which causes optical damage phenomena. The outgassing of organic molecules under vacuum conditions from any construction material like glue, ink and conductor boards can not prevented completely. So called laser induced contamination [5], [6], [7], [8] leads to damage formation on optical components within ADM-Aeolus operation time of 36 months. During this time the optical components have to withstand around 10^{-9} pulses, which can not be reached without any prevention mechanism of laser induced contamination. Laser induced contamination phenomena is not detected during irradiation under air atmosphere. Possible prevention can be caused by the presence of nitrogen or oxygen, whereas oxygen was identified as the dominated element for contamination prevention. For this reason, the ADM-Aeolus satellite will be pressurized for the mission with an oxygen pressure of 40 Pa [3].

1.2 Investigated topics of the thesis

The critical challenge of the laser induced contamination was already mentioned in the motivation part. Previous experiments by European Space Research and Technology Center (ESTEC) showed a positive effect of oxygen during laser irradiation under contamination atmosphere [9]. Influence of the partial pressure of oxygen was not quantified within previous experiments. The quantification of an oxygen threshold pressure will be the main challenge of this thesis.

Theoretical aspects of the thesis will be discussed in the chapter *Theoretical*

background of the thesis. At first the principles of the interaction between light and condensed matter are presented and focused to laser induced damage occurrence. Followed by the definition of laser induced contamination (*section 2.1*). Substantial aspects of optical coatings as well as an insight of production techniques are outlined *(section 2.2)*. The molecular nature of the contamination elements enables their in-situ monitoring with fluorescence microscopy. For this reason, a description of fluorescence phenomena is given (*section 2.3*).

The chapter *Test bench and measurement procedure* introduces the laser induced contamination test bench of the Institute of Technical Physics (ITP). Afterwards, the measurement procedures are presented (*section 3.1*). At first, a stationary method was used for a defined composition of an oxygen - contaminant atmosphere. Unfortunately, the adhesion of the contaminants on the vacuum chamber within the first minutes can not fulfill the requirements for tests lasting longer than 15 minutes. For this reason, the test bench was reconstructed and a dynamical method will be introduced. This one enables the in-situ monitoring of the partial pressures of oxygen and contaminants. Longterm tests under a defined partial pressure ratio can be performed.

The chapter *Results* is separated into a section regarding naphthalene as a contaminant model molecule and a section regarding spaceborne contaminants for the simulation of orbital systems.
It will be started with the naphthalene model. At first, positive aspects of oxygen are investigated and discussed with the stationary method (*section 4.1.1*). Followed by the dynamical method, a comprehensive view of the contamination challenge will be presented. A contamination experiment and a resulting damage phenomena without any partial pressure of oxygen within the measurement chamber will be shown. The quantification of an unknown oxygen - naphthalene threshold ratio is reached by the creation of various defined atmospheres. In-situ as well as ex-situ investigation methods are discussed and how the contamination purpose can be characterized. A threshold ratio was determined for low as well as for high fluences and longterm tests confirmed the positive oxygen influence (*section 4.1.2*).
The explored partial pressure threshold ratio arises the question, whether existing contamination structures can be cleaned by the irradiation under oxygen

atmosphere. High resolution in-situ monitoring enabled this procedure and the cleaning mechanism at low fluence is shown for different oxygen pressures *(section 4.1.3)*.

A model based coating was investigated considering the influence of laser induced contamination as a function of defect concentration within an optical sample. Two different gold nanoparticle interfaces were designed by the Laserzentrum Hannover (LZH) for the simulation of different defect concentrations compared to a reference sample. A partial pressure ratio of oxygen and naphthalene above the threshold ratio confirmed the positive influence of oxygen even at high defect concentration *(section 4.1.4)*.

To keep in mind, the advanced investigations of the laser induced contamination originates from the challenges with the ADM-Aeolus mission. A positive transformation of the investigation method to use a spaceborne contaminant was performed. The deposition of contamination during laser irradiation was proven as well as the cleaning mechanism at high fluence was investigated. As a key challenge, the prevention of laser induced contamination under the satellite's designed partial pressure configuration for oxygen is presented and this even for a high partial pressure of contamination *(section 4.2.1)*.

2 Theoretical background of the thesis

The following chapter is dedicated to theoretical topics concerning the influence of laser radiation on condensed matter, e.g. transparent materials. At first the characteristics of laser radiation will be discussed and how the radiation interact with condensed matter. Furthermore, electromagnetic perturbation of the lattice will be mentioned as well as the phenomena of optical surface ablation will be discussed. The ablation process, concerning optical samples, results in laser induced damage (LID) and the related quantity is called laser induced damage threshold (LIDT). Moreover, background of absorption processes will be presented and are discussed in further relation to the laser induced contamination (LIC). Optical coatings in high power applications are only designed for the used laser configuration, especially for satellite missions. The design of the coating has to consider the parameters of the laser (e.g. the wavelength). Outgassing of organic molecules of satellite systems in orbital position is a present challenge. Organic molecules interact with the optics surface. Fluorescence spectroscopy can monitor the molecules and can estimate qualitatively the deposition of contamination. Finally, a brief look at fluorescence mechanism will be presented.

2.1   Interaction between laser and condensed matter

Source of light for experiments is a pulsed laser. First laser system was developed by Maiman in 1960 [10], since then laser systems are used in a wide field of science. Today, there are many different systems available with a wide range of possible parameters. Parameters of the propagating light, what is the basis of the interaction between light and condensed matter, are the wavelength λ, the pulse duration τ, the fluence F (energy per area) and the intensity I (power per area). Whereas the last two parameters are calculated by the pulse energy, the beam profile as well as the beam shape and consequently they define the impinged energy per volume element into the condensed matter.

Pulse energy E_P, fluence F and intensity I are defined in the following way [11]:

$$E_P \quad = \quad \int_{-\infty}^{\infty} \int_{-\infty}^{\infty} F(x,y)\, dx\, dy \tag{2.1}$$

$$F(x,y) \quad = \quad \int_{-\infty}^{\infty} I(x,y,t)\, dt. \tag{2.2}$$

The spatial variables x and y span a Cartesian coordinate system orthogonal to the direction of propagation and t refers to the time. The Gaussian beam profile is given by:

$$F(x,y) \quad = \quad F_0\, e^{-2\left(\frac{x^2}{x_0^2} + \frac{y^2}{y_0^2}\right)}. \tag{2.3}$$

F_0 refers to the peak fluence and the variables x_0 and y_0 characterize the width of the Gaussian function and considering an elliptical shaped beam, the axes x and y of the Gaussian function fulfill the condition $F(x_0) = F_0\, e^{-2}$ and $F(y_0) = F_0\, e^{-2}$. Using equation 2.4 from [12, p. 466]:

$$\int_{-\infty}^{\infty} e^{-\frac{1}{2}x^2}\, dx \quad = \quad \sqrt{2\pi}. \tag{2.4}$$

the peak fluence can be determined from the pulse energy E_P:

$$F_0 = \frac{2E_P}{\pi\, x_0\, y_0}. \tag{2.5}$$

Assuming a radial symmetric beam along the axis of propagation and the width $\omega_0 = x_0 = y_0$, equation 2.5 can be transformed into cylindrical coordinates with

r as the distance from the optical axes:

$$F(r) = F_0 \, e^{-2\frac{r^2}{\omega_0^2}} \qquad \text{and} \qquad F_0 = \frac{2E_P}{\pi \, \omega_0^2}. \tag{2.6}$$

Temporal distribution of the intensity can be described for Gaussian pulses like $I(t) = I_0 \, e^{-4\ln(2)\frac{t^2}{\tau^2}}$ with the peak intensity I_0 and the pulse duration τ at FWHM. Inserting the intensity distribution into equation 2.2 and again using the relation from equation 2.4 the peak intensity is in relation to the peak fluence:

$$I_0 = \frac{2F_0}{\tau} \sqrt{\frac{\ln(2)}{\pi}}. \tag{2.7}$$

Linear absorption into a homogeneous media of an electromagnetic wave is characterized by the change of intensity along the axis of propagation z and is described by the Lamberts law [4]:

$$\frac{dI}{dz} = -\alpha I. \tag{2.8}$$

The material constant α [cm^{-1}] is a function of the wavelength and is called the absorption coefficient. Differential equation 2.8 yields an exponential decay with increasing penetration depths. At a given depth z the fluence $F(z)$ is given by:

$$F(z) = F_{\mathrm{in}} \, e^{-\alpha z}. \tag{2.9}$$

Lamberts law is valid for a homogeneous media and not for media with absorbers. The parameter α for different absorbing media (e.g. coatings) concludes of the particular absorptions coefficients α_i. Moreover, the Beer-Lambert law states, that the parameter α_i is proportional to the concentration c_i of the absorbers. Absorbance Δ_{abs} for a specified wavelength is described as the following:

$$\Delta_{abs} = \log \frac{I_{\mathrm{in}}}{I_{\mathrm{ex}}} = \alpha_i \, c_i \, z \,. \tag{2.10}$$

All mentioned parameters and values describe the properties of the laser beam and how the media decrease the energy density of the penetrating laser beam. Now, the physical principles and interactions of the laser beam and the media (e.g condensed matter) are discussed.

Interaction of a dielectric media is described in a classic theory by the influence of the electromagnetic wave on the elastic bounded electrons. Electrons are deflected against the atomic nucleus and the charge momentum is displaced,

what results in a dipole momentum. In other words, the electron feels the Coulomb force and the displacement is the origin of the electron's oscillation depending on the amplitude and frequency of the interacting electromagnetic wave. This effect is the so called polarization, which is for every media characteristic. Propagating wave equation of electromagnetic wave is still valid in media, but in absorbing materials the refraction index is complex, with an absorption coefficient α. Electrons in condensed matter absorb partially electromagnetic waves in the region of the near infrared up the to ultraviolet regime [4] and will rise the temperature, lead to thermal expansion, strain, movement of internal defects, cracking, melting and high shattering. Heating mechanism of the lattice comes from the electron - phonon interaction [13, p.43ff][14, p. 663ff], which induce thermal stress within the lattice. Assuming that all the absorbed energy E_{abs} is transformed in thermal energy Q to the volume element dV and no thermal diffusion is taken into account, than the deposited energy Q per pulse is:

$$\frac{dQ}{dV} \quad = \quad -\frac{dE_{abs}}{dV}. \tag{2.11}$$

Moreover, the absorption can be even increased by higher temperature due to the fact, that the change of the band tails of electronic states also change the transmission behavior of the material, which is described later on.

Influences of absorbing inclusions (inclusions are macro molecular particles and here only metal inclusion will be considered) are discussed in more detail for an improved understanding of damage occurrence. Figure 2.1 shows a strong dependence of the particle size as well as on the laser's wavelength to the laser induced damage threshold F_{LIDT}. Inclusions behave unique for every host material due to the thermal conductivity. A higher thermal conductivity K_h [$\mathrm{W\,cm^{-1}\,K^{-1}}$] of the host material will lead to a higher damage threshold relatively to the square root of K_h:

$$F_{LIDT} \quad = \quad \frac{6.2\,T_{cr}\,\sqrt{K_h}}{\gamma}\,\sqrt{3\rho_a C_a \tau}. \tag{2.12}$$

There, the critical Temperature T_{cr} sets the maximum temperature which can be reached by the irradiation, $\gamma = \sigma_{\mathrm{abs}}/\pi a^2$ is defined as the absorptivity relative to the diameter of the particle a and the cross section of the particle σ_{abs}, the density ρ_a and heat capacity C_a. Equation 2.12 neglects the thermal conductivity of the inclusion and respects a constant temperature of the metal
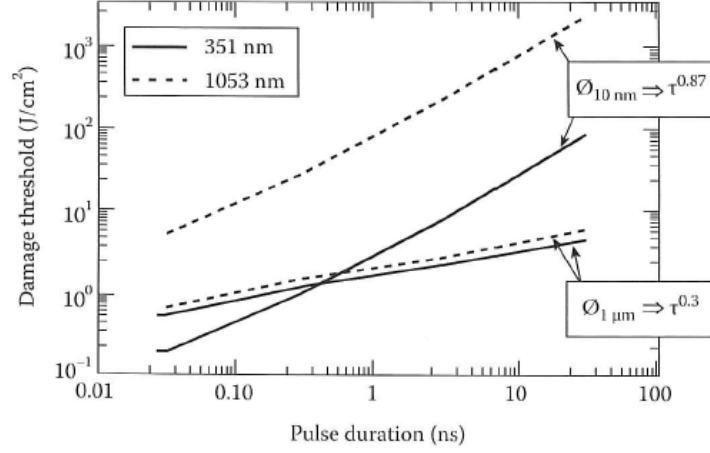
Figure 2.1: Comparison of damage threshold of 10 nm and 1 μm sized particle
with irradiation wavelengths of 351 nm and 1053 nm. The UV regime
shows decreased damage thresholds at least on magnitude for 10 nm
sized particles. Wavelength dependency decreases with increasing
particle size [13].

inclusion [13, p.34].

In principle, the cross section σ_{abs} quantifies the interaction probability between radiation and particle: the larger the cross section, the higher the interaction. In the first approximation, the imaginary part, what is related to the absorption, of the cross section for an inclusion can be written as:

$$\sigma_{\text{abs}} \quad = \quad \frac{24\pi^2 a^3}{\lambda_0} \frac{\epsilon_a'' \, n_h^3}{(\epsilon_a' + 2n_a^2)^2 + (\epsilon_a'')^2}. \tag{2.13}$$

The complex dielectric function of the absorber is $\epsilon_a = \epsilon_a' + i\epsilon_a''$ and n_h is the host refractive index. The wavelength of the electromagnetic wave in the host material is $\lambda_0 = \lambda \, n_h$ [13, pp.35-38].

Equation 2.13 is valid for small particles with diameters smaller than 20 nm. Moreover the shape of the absorbers influence the absolute temperature increase as well. Plate or rod like absorbers are more sensitive than spherical absorbers [13, p.39]. When the critical temperature T_{cr} of the absorber is getting higher than the melting temperature T_{melt} of the optical media (typically T_{melt} is between 1.5 - 3.0·10^3 K), a strong increase of the laser induced damage probability is determined. The high temperature of the absorber can melt the lattice of the host material, but this lead not automatically to a degradation

of transmittity. Different investigations [15], [16], [17] determined for damages, e.g. crack formation by metallic absorbers, a required temperature of approximately 10^4 K and the dimensions of the absorber should be larger than 100 nm [13, p.40ff]. Nevertheless, damages also occur on optics which are visibly free of absorbers, what leads to the assumption, that even very small (*a* smaller than 100 nm) absorbers lead to the cracking phenomena. This arises the idea, that small absorbers influence the nearby region with a high temperature increase what increases the energy absorption within the affected area. Papernov and Schmid [18] showed this effect quite impressively with deposited gold nanoparticle within a layer interface (see Figure 2.2).

Blackbody experiments by Carr et al [19] measured temperatures during laser
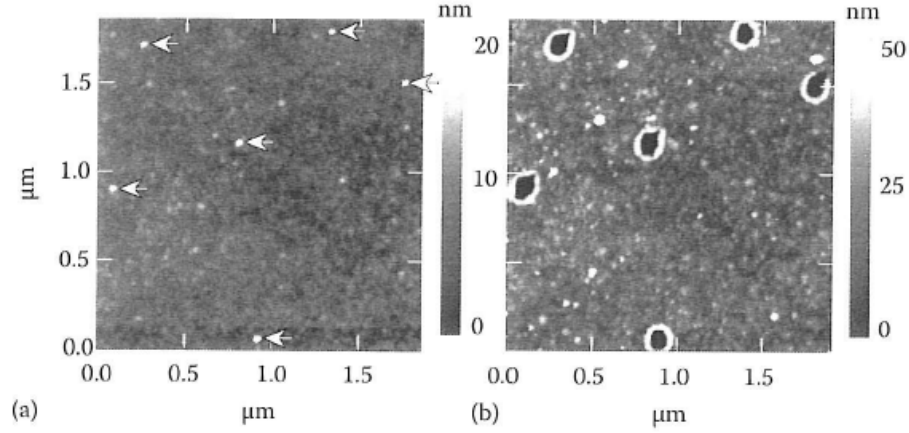
Figure 2.2: AFM images of SiO_2 optics with gold nanoparticle of average diameter from 1 - 20 nm. Arrows on the lhs indicate the position of the gold nanoparticle, embedded within a SiO_2 buffer layer. On the rhs, the same area after irradiation with 351 nm wavelength. Damage formation on the surface is obviuos [13].

damage phenomena of 8 - $12 \cdot 10^3$ K for different wavelengths and transparent host materials. Even though, there is no direct damage formation after the pulse, the risen temperature of local spots increases the probability of the electron transition from the valence band to the conduction band. The electromagnetic wave of the laser beam and unbound electrons can lead easily to avalanche ionization due to the fast interaction of 10^{-12} seconds [19] [20], what is a result of electron heating. This mechanism increases damage probability immensively. Grua et al [21] showed, that a high percentage of the free

electrons from metal particles can overwhelm the band gap of SiO_2. Another damage mechanism is discussed by Saito [22] as well as Bude [23] and refers also to the temperature effect. The material's transmission spectra changes due to higher lattice temperature and results in a lowered transmittance.

Now, the case will be discussed, where the absorbing particle is located near the surface. The physical behavior is not uniform anymore due to the surface layer. Consequently the physics are even more complex and chemical reactions from the atmosphere near the surface and their interactions have to taken into account. The intrinsic effect is the formation of crater structures due to absorbers (see Figure 2.3). Then, the characteristic of the surface is completely
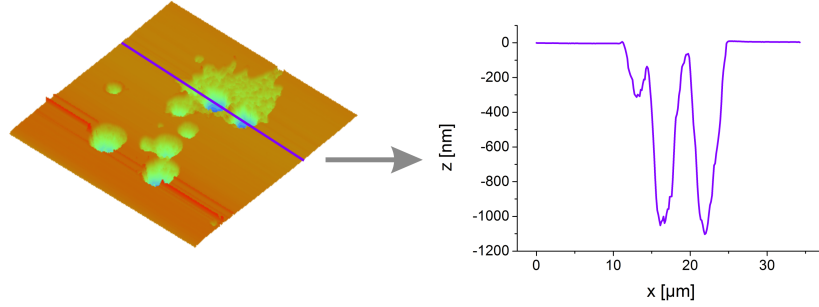
Figure 2.3: lhs: ex-situ DIC microscope of the exit side of an AR irradiated optic, rhs: corresponding AFM spectroscopy including the height profile.

different and scattering takes place. Such crack formation will induce stress and a shock wave leading to enhanced crack size [13, p. 48] [24], which is larger than the original size of the particle. All the defect spots, no matter if they are inside the media or on the surface enable electromagnetic field enhancement [13, p.5] [25].

Production processes of optical components are done within clean room facilities in order to avoid dust and reach high purity within the coating and bulk material. However, the optics feature a low number of defect vacancies at random positions. A statistical consideration [13, p.64ff] [26] can give an estimation of the probability to irradiate such a defect with a known beam diameter. Figure 2.4 illustrates the affected area which is relevant for the
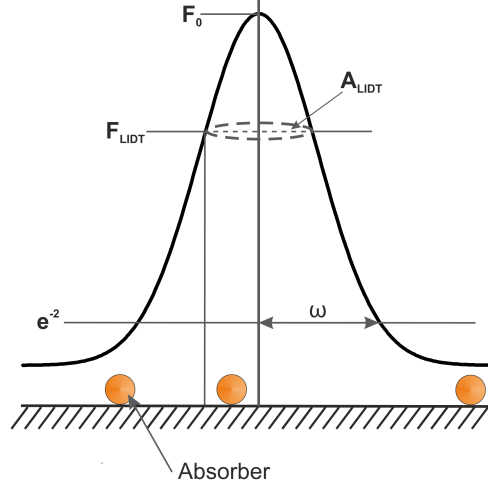
Figure 2.4: Laser beam with Gaussian like profile of maximum fluence $F_0 >$ F_{LIDT} with corresponding irradiation area. A_{LIDT} illustrates the area with irradiation fluences higher than F_{LIDT} and ω defines the half peak width to an intensity down to $1/e^2$.

irradiation A_{LIDT} and gives the equation:

$$A_{LIDT} \quad = \quad \frac{\pi\omega^2}{2} \ln\left(\frac{F_0}{F_{LIDT}}\right). \tag{2.14}$$

The Poisson distribution, postulating a constant and independent defect distribution with the defect density d, can be written as:

$$P \quad = \quad 1 - e^{-dA_{LIDT}}. \tag{2.15}$$

Combining equation 2.14 and 2.15, the probability of irradiating an absorber with similar or higher fluence than the threshold fluence is:

$$P(F_0) \quad = \quad 1 - \left(\frac{F_{LIDT}}{F_0}\right)^{\frac{\pi\omega^2 d}{2}}. \tag{2.16}$$

Obviously the probability is dependent on the beam spot size as well as on the defect density and the distribution from equation 2.16 requires that the damage thresholds of the defects are identical. To reach a high damage threshold, the defect density should be minimized.

Up to now, only particle contamination was considered. The particle contamination is identified as particles, which are an aggregation of a huge amount

of molecules. Whereas the molecular contamination considers only single molecules. Generally, such organic molecules are gassing out of construction
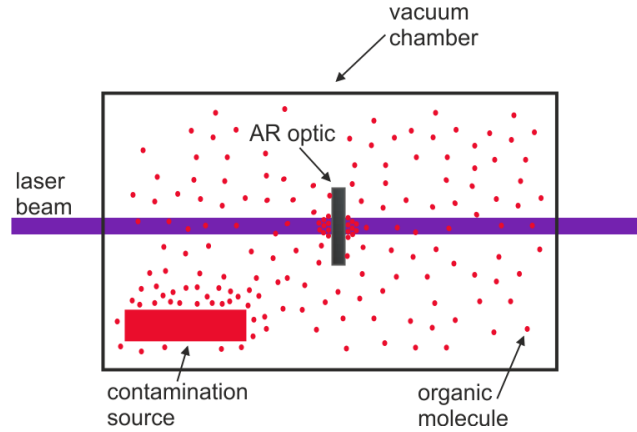
Figure 2.5: The outgassing molecules are highly deposited on the irradiated surfaces.

material like screw locks, ink or conductor boards and can adsorbe easily on the optics surface (see Figure 2.5). In principle, the outgassed molecules adsorbe homogeneous on the surface, but the laser beam increase the adsorption to the irradiation area due to the optical dipole force. Adsorbed molecules within the irradiation area interact continuously with the electromagnetic field of the laser beam. This interaction includes energy absorption on the optics surface. Deposited energy can lead to the same effects like discussed with absorbing particles. Institute of Technical Physics has demonstrated comprehensive expertise in previous work for the investigation of the formation of contamination as well as on the development of damage characterization [27], [28]. Deposition of contamination was shown confidentially for complex organic molecules, which were found in satellite systems. This contamination molecules, identified as spaceborne contaminants, are challenging to handle in terms of the unknown outgassing rate. As a model substance to simulate the contamination process naphthalene was identified. Naphthalene has an comparable chemical structure considering spaceborne contaminants and the high vapour pressure enables an easy manageable outgassing rate under vacuum conditions as well as a constant outgassing rate over a long time. This allows experiments lasting at least some hours without an inhomogeneous contamination pressure.

The investigated formation of the laser induced contamination happens already with low fluences at $100\,\mathrm{mJ/cm^2}$ and reduces the laser damage threshold by

at least one magnitude. Irradiation lasting million of pulses will form larger contamination spots with a pancake like profile, which will transform later to a doughnut profile. Increased absorptivity of the deposited contamination heats the surface up to the melting temperature of the dielectric optical medium. Crack formation can occur as well as ablation processes can start. In every state of the contamination process the quality of the optic is degraded and in strong cases the optic is damaged.

Moreover, the laser beam does not only affect the optical components and the adsorbed molecules on the optical surface, but also the molecules within the irradiated volume of the path way are influenced by the electromagnetic wave. Molecules can be excited, molecule bondings can be broken as well even ionization can occur with high power lasers. Photon's energy of $3\,\mathrm{eV}$ (corresponding to a wavelength of $355\,\mathrm{nm}$) in the UV regime excites oxygen molecules to higher vibrational states [29]. The excited oxygen molecule increases its reactivity to other molecules. The laser induced or laser supported chemical reaction of oxygen and contaminants leads to passive molecules like H_2O or $CO_{(2)}$. Poveda et al [30] investigated the molecule bonding behavior of naphthalene under irradiation of relevant wavelengths and pulse energies. It was determined the dissociation of naphthalene to excited benzene up to ionized molecule compounds (for our test system is an ionization not possible). The qualitative consideration of laser induced or supported chemical reaction is quite promising and have to be quantified in future work.

2.2 Manufacturing principles of optical coatings

Optical coatings have a high relevance for all kind of optical components, especially for high energy applications - starting from the coatings for mirrors, windows and thin film polarizer, just to name some of them. The desired robustness of these coating is getting even more important for systems with lack of any possibility to change the optical components. This is usually the case for satellites or space telescopes (service missions on the Hubble Telescope were quite exceptional [31]). During the thesis, just transmission optics were tested

and the following part will concentrate in special cases only on transmittive behavior and anti-reflective coatings.

Optical coatings follow the aim to minimize undesired optical effects like reflection for transmitting optics and transmission for reflecting optics. For high reflective optics the constructive interference condition should be met, by alternating layer deposition of high and low refractive indices (see Figure 2.6 for a schematic composition) [32, p.1-11ff and p.1-49ff]. The coatings are specified for each wavelength as well as incidence angle and are built up by a multiple of layers [13, p.343ff]. Transmitting optics have to fulfill the opposite condition - destructive interference.

At transmitting optics it have to take care about the entrance and exit face.
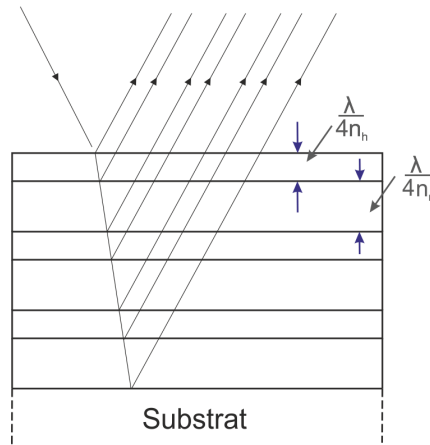
Figure 2.6: Schematic illustration for the composition of reflective coatings, n_h and n_n are the refractive indices of the layer.

From the logic of the ongoing wave and the Fresnel reflection at not coated dielectric optics, the energy density is higher at the incidental face than on the exit one and consequently it is expected that the entrance side shows damage behavior at first. But the opposite case was found. A reasonable picture is the fact, that the Fresnel reflection is $\pi/2$ out of phase on the entrance window and on the exit face is the electric field of the Fresnel reflection in phase to the laser radiation. This results to a higher net radiation on the exit face [13, p.5]. The so called field enhancement is the purpose of many investigations of defects, interface layers and surfaces at all, what was already mentioned above during the inclusion issue.

Now, the production procedure of optics is briefly described. There are different types of production techniques. The focus of the techniques is at the electron beam evaporation, the microwave supported magnetron sputtering and the ion beam sputtering. All production processes can be splitted into two major production steps - the material transport and attachment to the substrate [32, p.3-2]. The production cycles will be performed under vacuum conditions to avoid uncontrollable exposure from contamination of any kind [32, p.9-1].

Electron Beam Evaporation (e-beam)

The electron beam evaporation is a fast production technique and is widely used for surface coatings, especially for large area coatings like windows. An electron beam is aiming towards the target and evaporates the atoms and molecules, where the atoms will condense on surfaces in the direction of propagation. Kinetic energy of such evaporated atoms is in the range of tenth eV [33]. The chemical supported electron beam evaporation, where oxygen for metal oxides or acethylen for metal carbides are inserted to the chamber, sputters the metal target and the reactive gas will form oxides on the substrates surface [32, p.9-1ff]. Due to the low kinetic energy the layer deposition
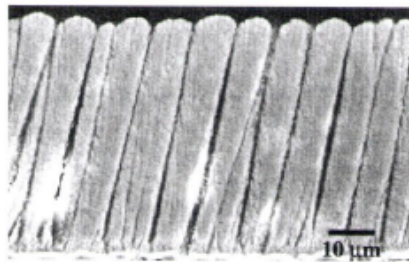
Figure 2.7: Perpendicular grain formation during e-beam coating process [34].

forms small rods or grains perpendicular to the substrates surface (see Figure 2.7). Surface porosity is quite high and compactness of the layer composition is about 90%. The compactness of a coating defines how dense the coating layer was deposited. A porous surface increases the adhesion of humidity, resulting into a change of the refractive index. Porous coatings can only be used under vacuum conditions to avoid the contamination with humidity. Compactness

could be increased to 97% by ion assisted deposition (IAD), where an ion beam (approximately $100\,\mathrm{eV}$) is aimed to the substrate and is colliding with the oxides during layer composing. Nevertheless, this additional process parameter breaks oxygen boundings within the layer, what lead to absorption centers in the UV regime [33].

E-beam process technique requires thermally stable substrates, because the substrates are heated to $300\,°\mathrm{C}$ [35] for an increased film adhesion and improved mechanical hardness of the layer. Additionally, the deposited oxide layer generates less absorption centers [32, p.9-6].

Magnetron Sputtering (MS)

The magnetron sputtered deposition technology MicorDyn$\textsf{®}$ invented by *Deposition Science Inc (DSI)* and in cooperational work with the *LASEROPTIK GmbH* was a microwave supported oxygen plasma attended. A sketched picture of the designed sputtering chamber is shown in Figure 2.8.

The argon ions of the magnetron plasma are accelerated to a kinetic energy
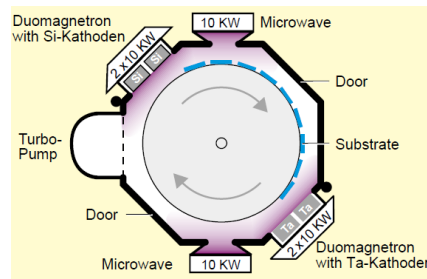
Figure 2.8: Schematic illustration of the magnetron sputtering chamber from Laseroptik GmbH [33].

on the order of $20\,\mathrm{eV}$ and sputters the atoms from the metal cathodes which will be oxidized in the argon - oxygen microwave plasma to metal oxides. The substrate holder within the chamber is rotating during the process and the argon - oxygen plasma filled the whole chamber, what is leading to a homogeneous layer composition. In former processes discharges occurred on the semi oxidized metal cathodes, which can be suppressed by the fast electrons of the microwave plasma as well as by the fast switching ($40\,\mathrm{kHz}$) magnetrons. All in all allows the combination of the duomagnetron- and microwave plasma

a comparable process time like conventional evaporation with better coating performance [33].

Ion Beam Sputtering (IBS)

IBS technology is deemed to be the advanced coating procedure regarding to high optical quality requirements. This process is able to minimize absorption effects down to 1 ppm for high reflective coatings for IR or to produce antireflective coatings with a rest reflectivity of lower than 10^{-4}. Basic principle of the process is illustrated in Figure 2.9. The implemented ion source with a
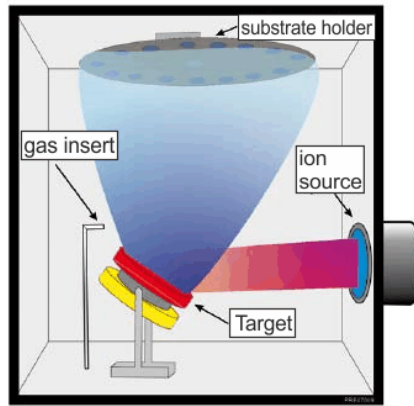
Figure 2.9: Schematic illustration of the IBS production process [35].

common acceleration of 0.5 keV to 2 keV sputters the metal atoms from the target. The sputtered coating atoms or molecules have a kinetic energy on the range of 10 eV to 20 eV and they will be oxidized during the layer composition with the help of an inserted oxygen atmosphere near the substrate. High kinetic energy of the coating atoms enables a dense agglomeration of the layer for high quality and stability. Additionally, the substrate holder is rotating during the deposition to increase a homogeneous deposition. Moreover, the process is due to the easy adjustment of process parameters stable and reproduceable as well as it enables a highly automated production line. Low temperature of less than 100 °C and low gas pressures allows to deposit the coating on sensible substrates as well as very low contamination effects will occur. Layer thickness is highly controllable down to nanometer scale due to the homogeneous sputtering and layer composition [35].

A process, independent from the coating deposition technique, is the post-cleaning of the surface. There are different kinds of cleaning methods for post processing of the substrate [13, p.317ff] as well as of the coated surface [13, p.375ff]. Concentrating on the substrate conditioning, any defects or scratches are principle precursors of LID respectively a lowered LIDT. After the substrate fabrication, the surface is polished to get a specified shape for the later application and/or specification. For example, the substrate is polished to a spherical geometry for light focusing and there are various different shapes. But the polishing process is in some cases a mechanical process and during the polishing process, particles from polisher can be embedded on the substrates surface. Such embedded particles are possible absorbers during irradiation. Investigations of Gorshkov [36] compared a regular polished interface with an interface, also polished but additionally evaporated with a thin copper layer of $1\,\mu$m. The laser damage threshold of the copper interface was far below the regular polished interface. Moreover, the investigations were performed with pulse durations in the nanosecond regime and have to be considered especially for the ADM-Aeolus mission.

Coating production techniques are challenging with different kinds of problems. This section presented just some of them to indicate the importance of high accuracy and clean production facilities.

2.3 Fluorescence phenomena

The fluorescence investigation and especially the fluorescence spectroscopy became an important method for various fields in science. Fluorescence phenomena can be found after the irradiation of common organic molecules. For this reason, fluorescence spectroscopy is used in a wide field of bio related topics as well as organic chemistry. To mention just some of the advantages - the high sensitivity, the simple preparation of the specimen and the characteristic spectra of the organic group are highly favorable. Fluorescence was first discovered and mentioned by Sir John Friedrich William Herschel on the surface of tonic water in 1845 [37]. The corresponding fluorescing molecule is quenine.

Since then, a lot of different fluorescence phenomena were discovered as well as mankind utilized the fluorescence in many fields of science [38, p.1-3]. For a detailed historical travel respecting fluorescence, the book from Berlman [39] is recommended.

Fluorescence signal will be generally presented in a spectra diagram with the
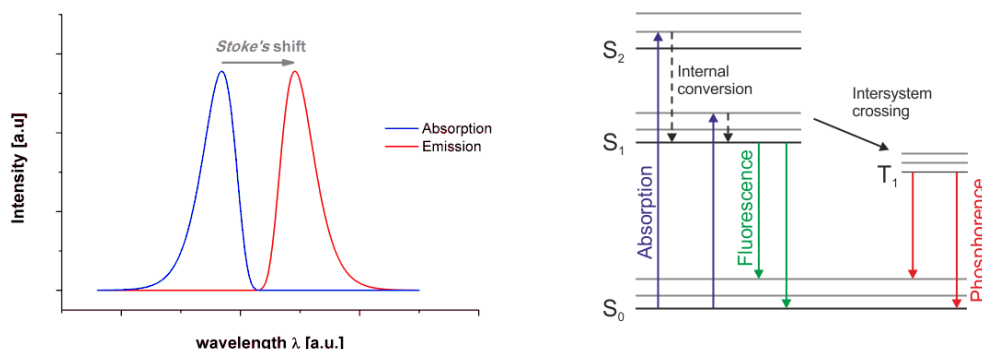
Figure 2.10: Characteristic fluorescence spectra and Jablonski diagram.

intensity corresponding to the wavelength of the light. The emission spectra is in most cases mirrored to higher wavelength from the absorption spectra (see Figure 2.10(lhs)). Absorption and emission lines are mostly discussed by using the Jablonski diagram [38, p.3ff]. Jablonski diagram illustrates the different electronic states of the molecules and also concludes the vibrational states respecting to the energy level. A typical Jablonski diagram is shown in Figure 2.10(rhs) including internal conversion and intersystem crossing. Fluorescence is categorized under the luminescence, which constitutes the emission of light from any media or substance. Besides the fluorescence there is the phosphorescence, both kinds emits light by relaxation from excited states onto the ground state. Fluorescence refers to excited singlet states (indicated in Figure 2.10(rhs) as S_i states) where the electron is paired by an opposite spin to an electron on the ground state. The process is so called spin-allowed and the relaxation time is in the region of 10^{-8} seconds. Whereas the luminescence is an excited triplet state (indicated in Figure 2.10(rhs) as T_i states), the states were attended via intersystem crossing, with identical spin situation what results in a spin-forbidden situation. Relaxation time increases immensively for these type up to hours (often used for night vision tools, e.g. self illuminated watch hands). The already mentioned shift of the spectra wavelengths be-

tween absorption and emission was first discovered by Sir G.G. Stokes in the
year 1852 [40] and is named as the Stokes-shift (see also Figure 2.10(lhs)).
Explanation for the frequency shift is due to the fast relaxation of about 10^{-12}
seconds of the vibrational states (keep in mind, that the fluorescence relax-
ation is in the time range 10^{-8} seconds), what is a thermally effect. A chance
of the Stokes-shift can be caused by other substances like the kind of solution
were the fluorescing molecules are embedded and also the solvent concentra-
tion, on possible excited state reactions and/or on energy transfer within the
molecule and/or to any solvent. Another interesting fact corresponding to
the fluorescence spectra is, that the emission frequencies are, except for some
materials due to their electronic state levels, independent from the absorption
frequencies [38, p. 3ff]. This effect is described by the internal conversion of
the excited states and was reported by Varilov [39] and Kasha [41].

Another characteristic parameter of the fluorescence despite the spectra is the
lifetime τ_{Fl} as well as the quantum yield Q. The quantum yield represents
the relation between the number of absorbing Γ_{ab} and emitting Γ_{em} photons.
Indifference between Γ_{ab} and Γ_{em} is defined as a non-radiative decay k_{nr} and
the quantum yield is given by:

$$Q = \frac{\Gamma_{\mathrm{ab}}}{\Gamma_{\mathrm{em}} + k_{\mathrm{nr.}}} \tag{2.17}$$

Additionally, the fluorescence lifetime τ defines the meantime during the elec-
tron remains at the excited state. Lifetime τ is qualitatively a random process
and gives only an average time. Usually, the fluorescence lifetime is in the
$10\,\mathrm{ns}$ regime [38, p.8-10].

Besides the radiative relaxation of the excited state there is also the possibility
of relaxation due to interaction with other unaffected molecules in the nearby
region, so called quencher. Quenching reduces the emission rate or can change
the Stokes shift to even higher wavelengths. Collisional quenching is based
on charged exchange between the molecules which was not represent on the
ground state or allows the possibility of intersystem crossing which can lead
to phosphorescence effect. Quenching mechanism will not change the con-
centration or the chemical identity of the quencher. Stern-Volmer equation
quantifies the collisional quenching in relation of the nominal photon flux F_0
and the photon flux in presence of quencher F:

$$\frac{F_0}{F} = 1 + K[Q] = 1 + k_q \tau [Q]. \tag{2.18}$$

The Stern-Volmer quenching constant K indicates the sensitivity of the fluorescing molecule to a specific quencher, K_q is the bimolecular quenching constant and Q is the concentration of the quencher. Equation 2.18 allows the possibility to quantify the concentration of quenching molecules, e.g. for oxygen sensors. Enabling quenching effects, the quencher has to be in the direct region of the fluorophor. That means for fluorescing molecules which are embedded in a solutions, the quencher has to be in the region within the distance of the diffusion length Δx^2 for the fluorescing time regime τ of 10^{-8} seconds and the diffusion constant D [38, p.11]

$$\Delta x^2 = 2D\tau. \tag{2.19}$$

As already mentioned above, the fluorescence spectroscopy is highly used in biological as well as in medical fields of science. Fluorescence anisotropy is used for the characterization of macromolecules within cells. The origin of the effect is, that the photon absorption is more likely, when the electromagnetic vector of the photon is parallel to the transition momentum of the fluorophore. The emitted light will also depend on the transition moment of the fluorophore. But it has to be taken into account, that average fluorescence lifetime is on the order of 10^{-8} seconds what is large compared to rotational decay of molecules in solvents (about 10^{-10} seconds). The rotational velocity slows down immensively when the molecules are bounded or corporated within a cell structure. Then both time scales are comparable and the spectroscopy can extract the bounding conditions. This information can derive the (health) status of the cell and/or their biological activity [38, p.12-13].

Laser systems with wavelengths in the region of visible or UV light can be used for the excitation of organic molecules. The high stability of the laser irradiation allows a constant excitation rate for qualitative and quantitative fluorescence spectroscopy. An identified source enables the possibility of concentration as well as chemical reaction investigations. Whereas a change in concentration will change the signal intensity (see the Stern-Volmer equation 2.18), chemical reaction will change the fluorescence spectra [43, p.105ff]. Here, the fluorescence spectroscopy enables the possibility for dynamic reactions, where the concentration of involved molecules can be varied over time, e.g.
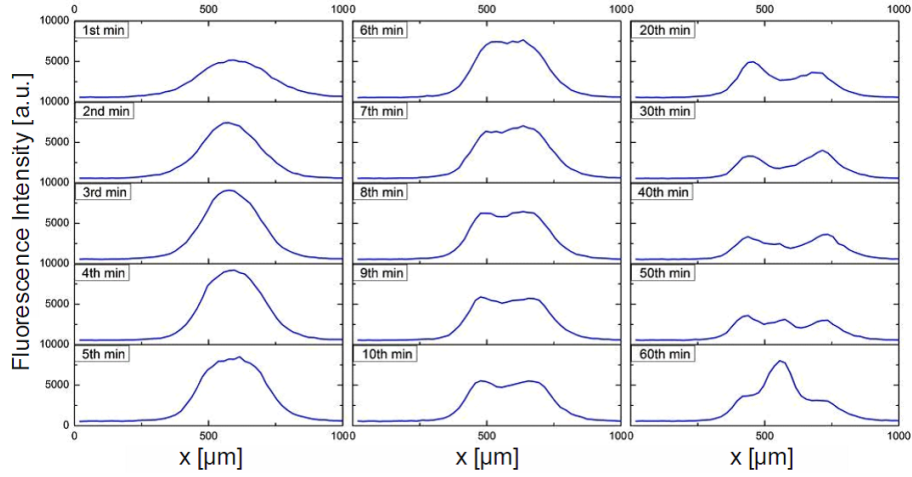
Figure 2.11: In-situ fluorescence monitoring over time of laser induced fluorescence under irradiation of e-beam coating under $3.5 \cdot 10^{-4}$ mbar naphthalene pressure and $0.6\,\mathrm{J/cm^2}$ with repetition rate of $1\,\mathrm{kHz}$. Transition from pancake to doughnut structure visible [42].

combustion processes can be optimized with the laser induced fluorescence tool [44]. In the case of laser induced contamination the intensity signal gives an impression of the molecular activity on the optics surface (backscattered laser light is filtered via 400 nm edge filter) as well as on the grown up geometric of deposited contaminants over time (Figure 2.11). Ultra short pulse lasers (Femtosecond lasers) can even induce multiphoton absorption for more complex molecule analysis [43, p.113ff].

3 Test bench and measurement procedure

The test bench at the Institute of Technical Physics (ITP) is designed to match the on board working conditions of the ADM-Aeolus satellite. Because there is no standardized design, the LIC test bench is designed by the ITP and was extended and upgraded to the current setup, which is shown in Figure 3.1.

Laser System   The laser source is a diode pumped Nd:YAG laser with a nominal wavelength of 1064 nm, pulse duration of 10 ns and a repetition rate up to 1 kHz. All the presented experiments were performed with the repetition rate 1 kHz. Frequency tripling implementation delivers an output wavelength of 355 nm. Pulse energy can be altered by the Q-Switch delay and the attenuator within the beam line, consisting a $\lambda/2$ plate and a thin film polarisator. Laser beam is splitted into 4 equivalent beams and the sample holder is designed such three optics can irradiated simultaneously and the 4 th beam is used as a reference signal. Energy detectors behind the samples enables in-situ transmission measurement. The UV beam of the Nd:YAG laser has a Gaussian profile with a $1/e^2$-diameter of 250 μm and is focused onto the sample holder. Focus point of the beam is not perfectly shaped, but the Gaussian intensity fit of the beam profile (Figure 3.2) matches the desired beam diameter quite well.

UHV Chamber System   UHV chamber allows with its flexible design many investigation possibilities. The chamber is pumped by a turbo molecular pump
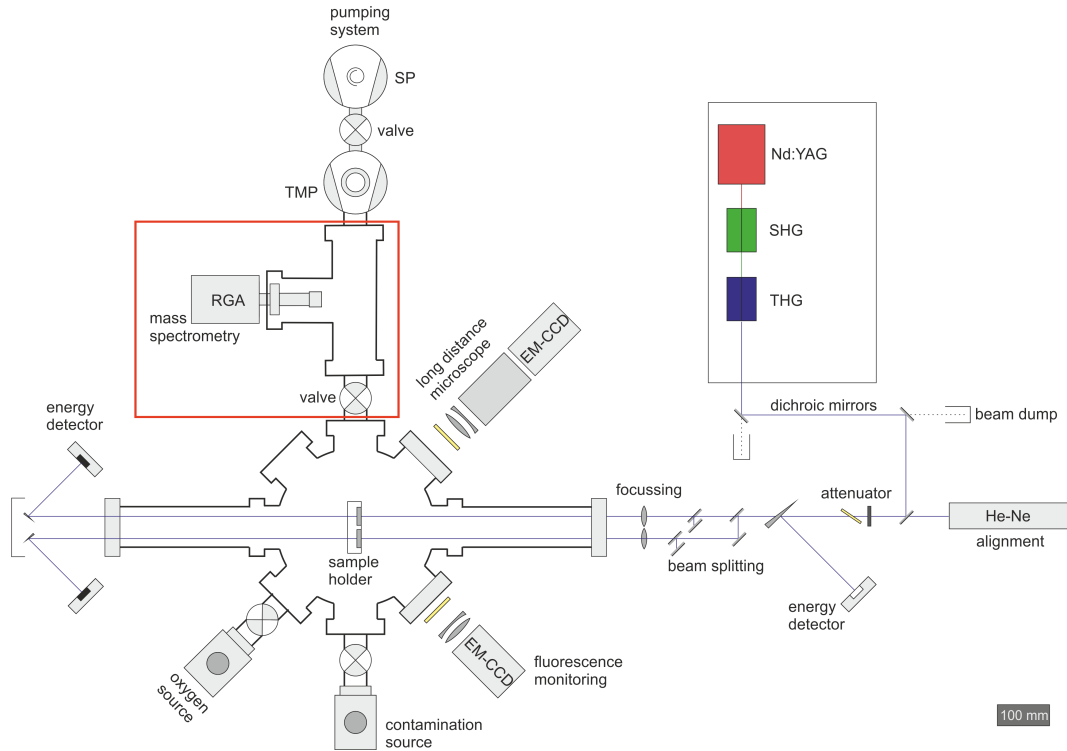
Figure 3.1: Laser induced contamination test bench with the implemented differential residual gas analyzer (RGA).

(TMP) and an oilfree scroll pump. Differential pumped residual gas analyzing chamber (diff. RGA, red encircled in Figure 3.1) is separated via a gate valve from the science chamber. The gate valve enables a flexible outflow alignment and is highly needed for a defined contamination atmosphere. Another advantage of the gate valve compared to a needle valve is the possibility of a fast pumping mode. Pirani, Penning and capacitance manometers are implemented for pressure sensing in both chambers. The heated contamination source is connected via a needle valve to the main chamber and can be filled with different kind of contamination material. For contamination and damage prevention are the laser entrance and exit windows heated to 150 °C. Moreover, the adjustment of the kaustic leads to lower fluence on the window positions.

In-situ measurement system   In-situ image system is highly necessary for the investigation of deposition and ablation processes. An EM-CCD camera (Andor Luca) was equipped with the long distance microscope (LDM). The
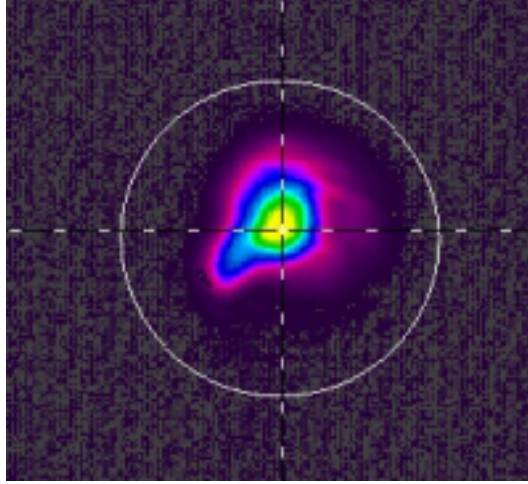
Figure 3.2: Laser beam profile on the optics surface.

EM-CCD (LDM) camera can be triggered in two different modes - as a bright-field surface microscope and as a fluorescence camera. Bright-field surface microscope mode involves a simultaneously triggered flashlight lamp. Fluorescence mode activates the electron multiplying system of the CCD chip and enables the possibility to measure low intensity (fluorescence) light. Uncorrected images of the in-situ surface microscopy and in-situ fluorescence images are shown in Figure 3.3 for a typical non-damage (upper row) and damage occurrence (lower row). The scattering light from the laser is blocked with a 400 nm edge filter. Overall resolution of the EMCCD (LDM) camera is 5 - 10 μm. Another camera, also a EM-CCD camera (Andor Luca) is attached onto a stage movement system. This allows the sequential fluorescence investigation of all three samples. This EM-CCD is equipped with a conventional zoom-objective, so the resolution is lower than the LDM system

Transmission is measured in-situ with energy detectors (PD10v2 from Ophir). With the help of a fifth detector is the pulse energy of the laser before beam-splitting measured. Variation of the pulse energy over the time can be tracked and for further transmission analysis the variation of the laser can be corrected. A typical energy corrected transmission curve is shown in Figure 3.4 as well as the pulse energy. Implemented energy detectors, which are basicly Si-photodiode sensors, are not cooled or thermally stabilized in any way. A variation of the detectors temperature will also effect the CCD sensor, what

(a) Surface microscopy

(b) Fluorescence microscopy

(c) Surface microscopy

(d) Fluorescence microscopy
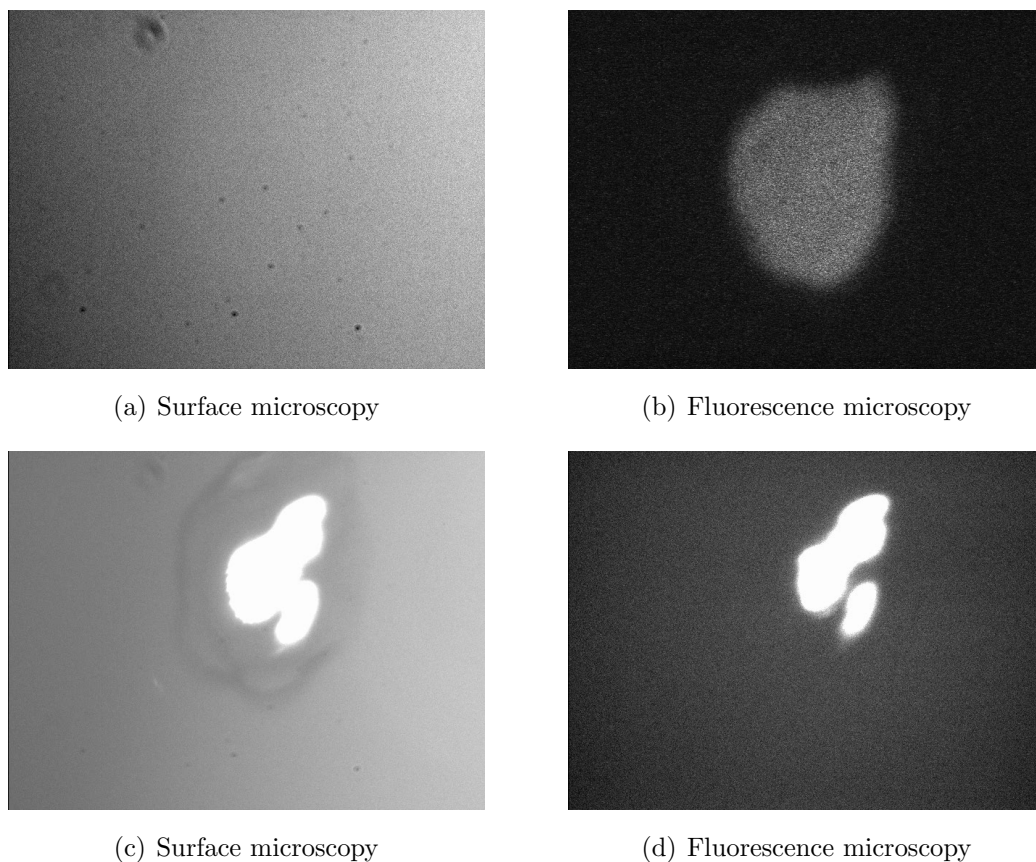
Figure 3.3: Typical in-situ LDM images for non-damaging behavior (upper row) and damaging behavior (lower row).

can result in a small error on the detected pulse energy over time. Nevertheless the lab is air conditioned providing a constant temperature. Because the transmission is corrected by a detector of the same type, the temperature effect can be minimized. But every chip has its own characteristic, even when they are calibrated, so residual temperature instabilities remain.

RGA system from Stanford Research Systems can measure atomic masses up to 200 amu, what is essentially for tracking even high mass molecules. The system uses a quadrupole mass filter and Faraday cup detector as well as for very low pressures an optional electron mulitplier. It can identify the composition to a pressure up to 10^{-4} mbar. A calibration check for the partial pressure of oxygen respecting to the total pressure in the diff. pumped RGA
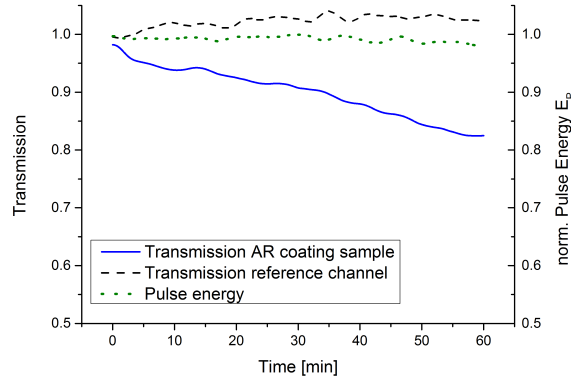
Figure 3.4: Independent in-situ transmission of the samples transmission and the reference signal. Normalized pulse energy signal as consideration of stable condition.

chamber system was performed. RGA is a very powerful instrument to measure relative concentrations between the elements. Consequently the relation between oxygen and contaminant can be related to the absolute pressure of the element within the chamber. It can perform a full range measurement up to 200 amu, what is exemplary shown for naphthalene in Figure 3.5(a), or it can be a pressure vs time measurement of selected elements (maximum 8 elements) performed. This is important for the time tracking of the oxygen - contamination atmosphere and is shown for a 4000:1 ratio in Figure 3.5(b).

3.1   Measurement procedure

Main purpose of this thesis is the investigation of the oxygen influence to the laser induced contamination with oxygen pressures up to $40\,\mathrm{Pa}$. Contamination experiments were usually done in the pressure range of $10^{-5}\,\mathrm{mbar}$ (or $10^{-3}\,\mathrm{Pa}$). Consequently a gate valve was installed between the chamber and the TMP. This allows stationary contamination experiments under oxygen atmosphere.

(a) full range measurement

(b) pressure vs time mode
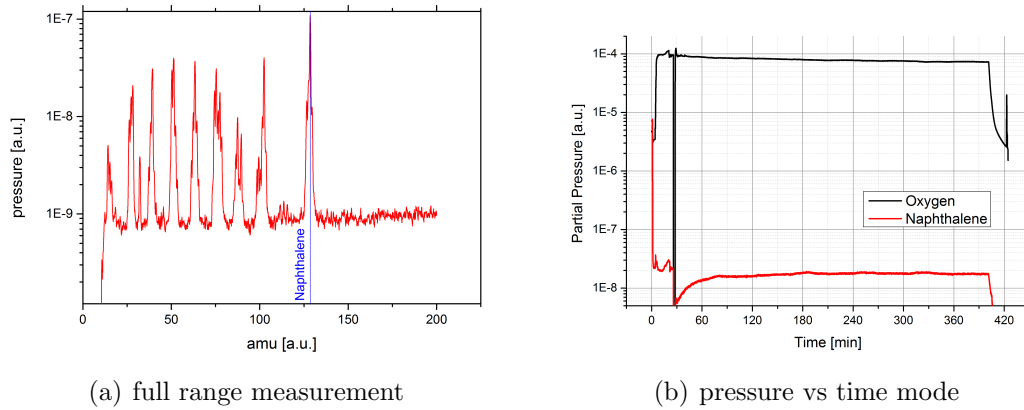
Figure 3.5: Principle RGA measurements for the full range mode up to 200 amu and the pressure vs time mode, typical atomic mass spectra of naphthalene and oxygen - naphthalene atmosphere with the partial pressure ratio 4000:1.

Stationary contamination procedure   In order to provide a defined oxygen-contaminant atmosphere, the need of the RGA system is indispensable. During the stationary experiments was the RGA implemented directly on the science chamber. The preparation sequence is to fill the chamber with a defined contamination pressure. Afterwards, the gate valve and the needle valve from the contamination source are closed simultaneously. Now, oxygen is filled into the chamber and the chamber can be pressurized up to normal pressure. This is a fast and easy way to create an oxygen - contamination mixture. But it has to be considered, that the gas mixture can not be monitored during the experiment sequence, because the RGA operates only until 10^{-4} mbar. This is a great issue for tests lasting longer than 20 or 30 minutes. Investigations of the adhesion time of naphthalene onto the chamber wall arisen an adhesion time of around 15 minutes. After that time, the contamination pressure is not equivalent anymore.

The limited measurement time is a high challenge for longterm experiments. Because it is necessary to fulfill the requirements of experiments lasting at least 1 h, the test bench was upgraded to the differential pumped system.

Dynamic contamination procedure   As mentioned above, the continuous of an equivalent contamination pressure is essential for the experiments. The implemented differential RGA can fulfill the requirements and it was tested and calibrated to the test bench. Continuous monitoring allows the calibration of a defined mixture of the oxygen - contaminant atmosphere. Experiments work flow follows the major steps: after a desired ratio of the oxygen and contamination partial pressure is adjusted, the gate valve is closed until the desired atmosphere pressure is reached. During the adjustment of the partial pressure ratio, the partial pressures are down to 10^{-8} mbar, that's why the gate valve will closed to get higher absolute pressures of oxygen and contaminant. After the science chamber is pressurized, the partial pressure of the contaminant is in order of 10^{-5} or 10^{-4} mbar. At last, the gate valve will be opened again to achieve constant pressure in the science chamber and the gaseous inflow and outflow is similar. This allows a constant contamination atmosphere over the irradiation time, due to the infinity among of outgassing naphthalene.

4 Results

Results of the oxygen influence on laser induced contamination are presented in the following chapter. At first, the experiments with naphthalene as contaminant are presented. Additionally, laser induced cleaning mechanism is investigated for cleaning LIC depositions after their formation. The influence of particle inclusions were investigated with artificial produced particles, which were embedded in the coating. Furthermore, the irradiation condition of transmitting optics in satellite systems were simulated with a specified spaceborne contaminant.

4.1 LIC experiments with naphthalene

For the investigation of oxygen, various parameters like the variation of the fluence, absolute contamination pressure as well as the oxygen - contaminant concentration were tested and their influence on the optical component was determined.

4.1.1 Stationary laser induced contamination

The test parameters are listed in Table 4.1. Due to the high number of tests, only selected measurements will be presented. The list of the performed measurements is shown in the appendix.

Figure 4.1 shows the transmission behavior under irradiation with the fluence $0.9\,\mathrm{J/cm^2}$ over 60 minutes. The two coating types, e-beam and MS show almost similar behavior for each oxygen pressure - $1\,\mathrm{Pa}$ and $10\,\mathrm{Pa}$. Experiments

Parameter	
Fluence [J/cm^2]	0.3, 0.6, 0.9
Naphthalene pressure [mbar]	$4 \cdot 10^{-5}$, $8 \cdot 10^{-5}$
Oxygen pressure [Pa]	0, 1, 10, 40
Coating types	MS, E-Beam, uncoated SiO_2

Table 4.1: Variation of the experimental parameters under stationary contamination conditions.

without oxygen and equivalent parameters are not shown, but the damage formation was in-situ as well as ex-situ obvious. The difference between 1 Pa
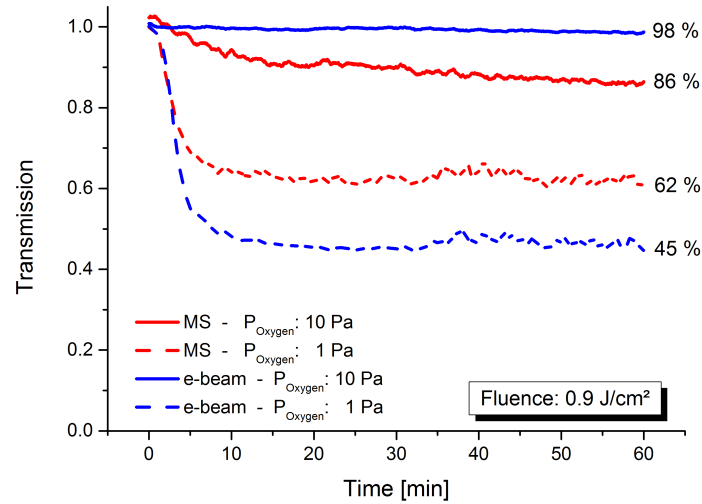
Figure 4.1: Influence of oxygen pressure variation on MS and e-beam antireflective coatings with naphthalene pressure of $4 \cdot 10^{-5}$ mbar and the fluence 0.9 J/cm^2.

and 10 Pa of oxygen is significant: the 10 Pa oxygen test prevents a strong transmission degradation, but the transmission degrades very strong in the first minutes at the experiment with 1 Pa oxygen. If the transmission degrades, this happens always within the first 10 - 15 min. Afterwards it is almost no transmission change noticeable. Former tests [28] showed ongoing transmission loss over the whole irradiation time. But these experiments were performed without oxygen and the contamination material was inserted and

(a) DIC

(b) ex-situ fluorescence
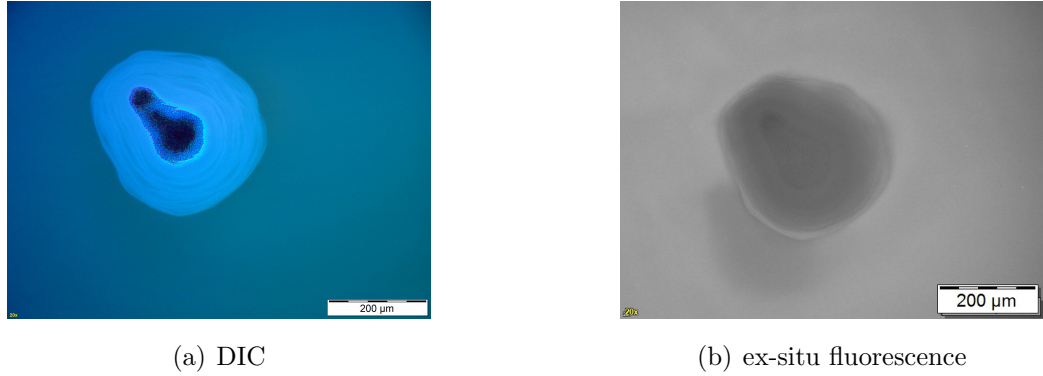
Figure 4.2: Ex-situ differential interference contrast (DIC) and ex-situ fluorescence microscopy for the entrance face of the e-beam 1 Pa oxygen experiment with a partial pressure of naphthalene $4{\cdot}10^{-5}$ mbar and the fluence 0.9 J/cm^2. Ablation area at high fluence region is obvious. Fluorescence is also influenced by the whole irradiation area.

pumped down continuously, what means, that the contamination pressure and atmospheric composition was constant over the irradiation time. Differential interference contrast (DIC) as well as fluorescence were measured ex-situ and is shown in Figures 4.2 and 4.3 for the e-beam experiment with 1 Pa and 10 Pa oxygen. The DIC shows for the 1 Pa oxygen experiment a strong damage on the irradiated surface area, ablation is in advanced state, what is also visible

(a) DIC

(b) ex-situ fluorescence
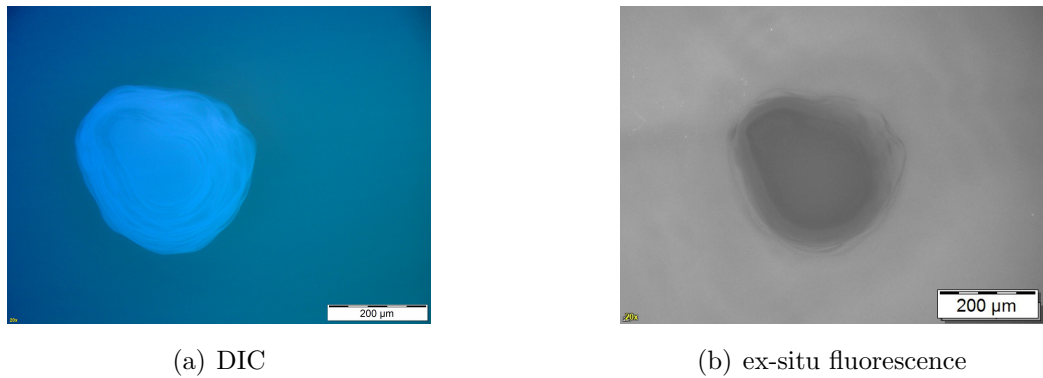
Figure 4.3: Ex-situ DIC and fluorescence microscopy show no ablation phenomena for the e-beam 10 Pa oxygen experiment with a partial pressure of naphthalene $4{\cdot}10^{-5}$ mbar and the fluence 0.9 J/cm^2. But deposition is visible on the irradiated surface.

in the degraded transmission. In-situ fluorescence measurement confirms the ablation process, which starts shortly after the irradiation started (see Figure 4.4 - red line). The deposition of contamination on the surface leads to an increasing in-situ fluorescence signal. Afterwards, the ablation process started and the fluorescence signal remains high. But it has to be considered, that in case of ablation other processes, e.g plasma formation, may contribute to measured intensity.

The 10 Pa oxygen experiment shows a deposition on the surface. Deposition
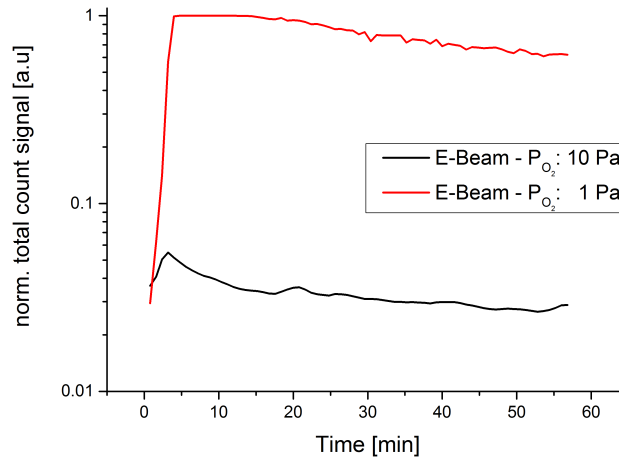
Figure 4.4: Normalized total count signal of in-situ fluorescence microscopy (background corrected) for the e-beam 10 Pa and 1 Pa oxygen experiment.

area is larger than the beam diameter of around $250\,\mu$m, what means, that also the surface is affected by the laser-induced contamination by laser energies below the $1/e^2$ condition. Although the deposition is visible in the ex-situ images, the transmission line is almost unaffected. In-situ fluorescence shows a low intensity, what indicates that no strong deposition or ablation took place and the transmission curve supports a non-ablation process.

Following scanning electron microscope measurement were performed at the TU Dresden. This SEM can only be used in high vacuum mode. To prevent charging of the non-conductive samples, they were sputtered with a conductive Au-Pd layer of about $5\text{-}10\,\mu$m. Nevertheless it could not be excluded any inhomogeneity of the Au-Pd deposition.
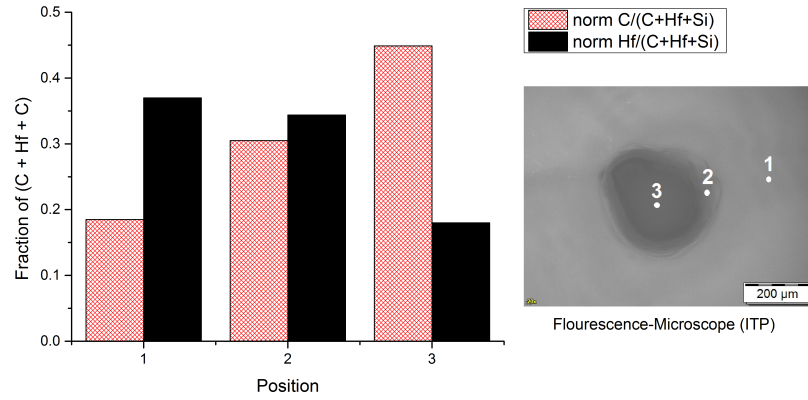
Figure 4.5: Normalized element concentration of carbon and hafnium on the left hand side for the e-beam 10 Pa oxygen experiment. Ex-situ fluorescence at the right hand side indicates the investigated positions.

The element concentration of carbon and hafnium (hafnium was used as coating material) at various positions can be seen in Figure 4.5 for the e-beam 10 Pa oxygen experiment and in Figure 4.6 for the e-beam 1 Pa oxygen experiment. The fluorescence picture within the figure are the same images shown above and they shall indicate the investigated positions.

The concentration of carbon at the e-beam 10 Pa oxygen experiment increases with decreasing distance from the center of the laser beam. Consequently, the
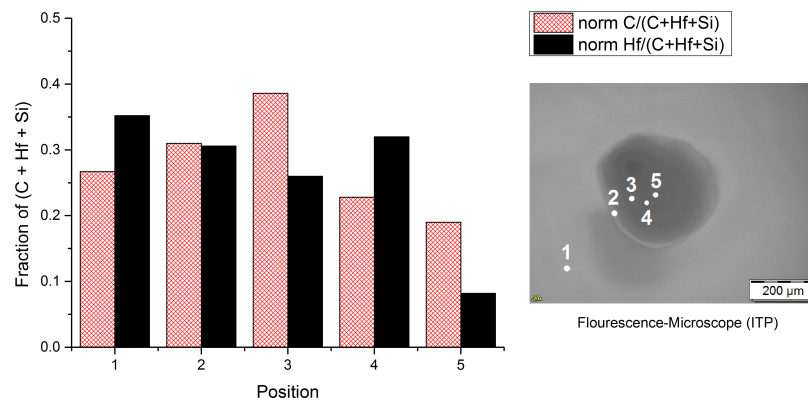
Figure 4.6: Normalized element concentration of carbon and hafnium on the left hand side for the e-beam 1 Pa oxygen experiment. Ex-situ fluorescence at the right hand side indicates the investigated positions.

deposition of carbon increases with higher fluences.

Carbon concentration of the e-beam 1 Pa oxygen experiment shows a doughnut-like profile. Carbon distribution is for doughnut-like profiles lower in the center of the laser beam than in the surrounding area. As mentioned above, the fluorescence, the DIC measurement and transmission show strong damage behaviour due to the ablation process.

Moreover the high fluence of the Gaussian laser beam showed in the high magnification SEM image of the 1 Pa oxygen experiment periodic surface ripples on the substrate (see Figure 4.7). The ripples are separated of around 250 nm, what corresponds to interference effect by the irradiation with a wavelength of 355 nm.
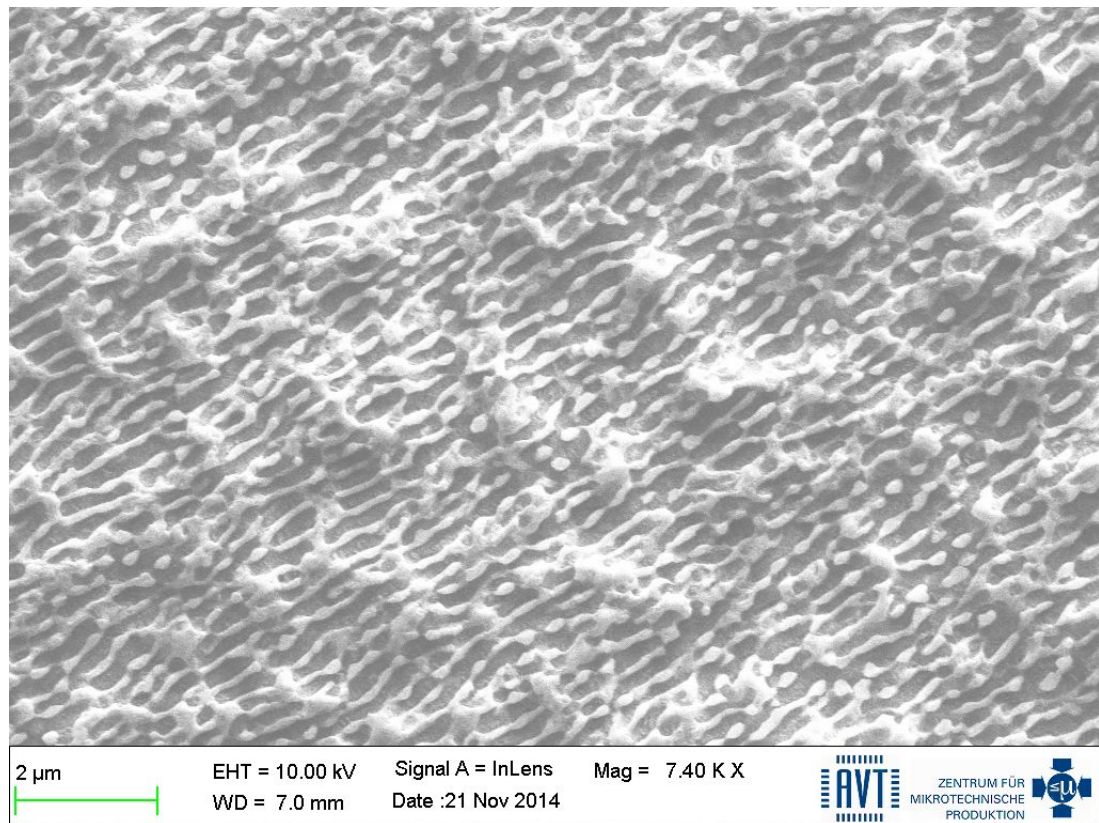
Figure 4.7: Periodic surface ripples within ablation area of the e-beam 1 Pa oxygen experiment.

4.1.2 Dynamic pumped contamination atmosphere

The implementation of the differential pumped RGA system enables the possibility of a continuous tracking of the contamination atmosphere. Also the adjusting of oxygen for defined oxygen - naphthalene ratios is essential for the determination of a threshold pressure of oxygen. Experiments were performed with equivalent parameters like the stationary contamination experiments and are listed in Table 4.2. A repetition rate of $1\,kHz$ was used for all the tests

Paramter	
Fluence [J/cm^2]	0.3, 0.6, 1.0
Naphthalene pressure [mbar]	$1 \cdot 10^{-5}$, $1 \cdot 10^{-4}$
Oxygen - Naphthalene ratio	0:1, 10:1, 50:1, 100:1, 1000:1, 4000:1
Coating types	MS, E-Beam, uncoated SiO_2, IBS (longterm test)

Table 4.2: Variation of the measurement parameters under dynamic pumping procedure.

and achieves the possibility of a shorter testing time with respect to the absolute pulse number (- mostly the tests lasted 3.6M pulses, corresponding to 60 minutes of irradiation).

In-situ transmission measurement in combination with the in-situ fluorescence monitoring as well as the surface microscope monitoring allows time resolved investigation of laser induced contamination. Now, an exemplary presentation of damage formation due to laser induced contamination is presented. This experiment was performed under a contamination atmosphere, without any oxygen. Figure 4.8 shows the in-situ transmission during irradiation of a magnetron sputtered antireflective optic with a fluence of $1\,J/cm^2$ and a naphthalene atmosphere of $1 \cdot 10^{-5}\,mbar$ for $60\,min$. This is much lower than the laser induced damage threshold fluence of $6.9\,J/cm^2$.

In-situ transmission degrades within the first minutes and the in-situ fluorescence on the right hand side of Figure 4.8 (Inset 1- 3) increases immensively
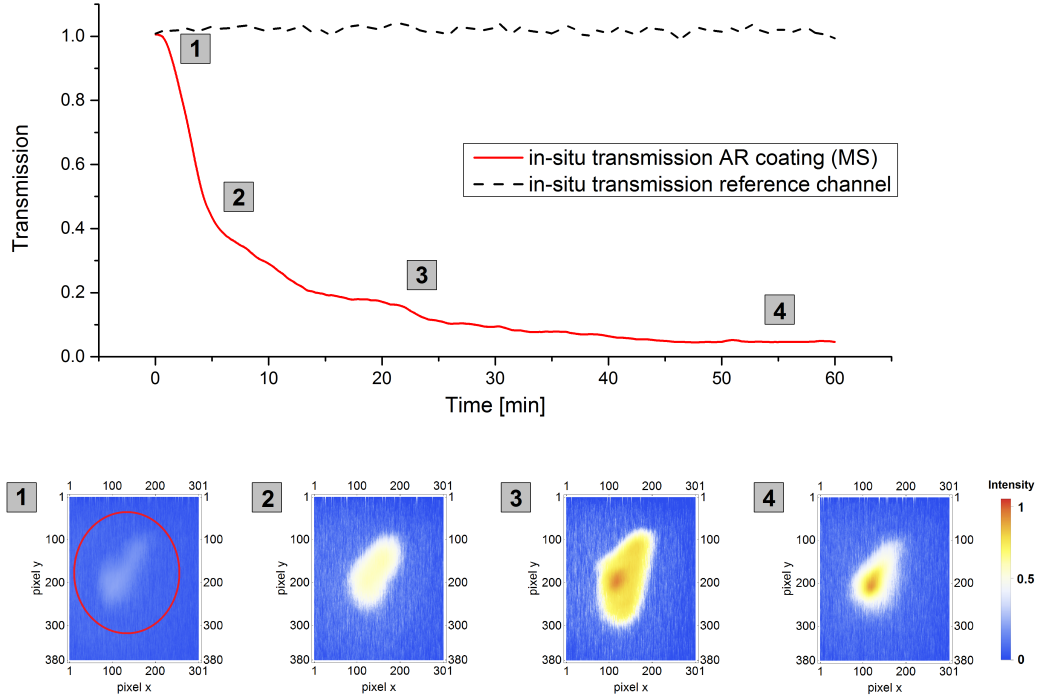
Figure 4.8: Upper row: in-situ transmission of magnetron sputtered antireflective optic with a naphthalene pressure of 10^{-5} mbar and the fluence $1 \, \text{J/cm}^2$. Lower row: in-situ fluorescence (LDM), the images are background corrected and scaled identical. The red circle indicates the irradiated area.

and saturates after 25 minutes of irradiation. The fluorescence insets correspond to the signal of the long distance fluorescence camera. Again, after the ablation process started, the probably contribution of plasma is holding the cameras signal high. The signal of the fluorescence camera is related to depositing and ablating processes. Because the deposition of contamination leads to increased absorption, the surface is heated up by the laser irradiation and when the surface temperature gets too high, the ablation process is started. Obviously contamination should be avoided to keep the damage threshold high. In contrast to the in-situ fluorescence the in-situ surface microscope is used for investigation of the surface morphology. It is shown in Figure 4.9 and corresponds to the same time stamps like the in-situ fluorescence pictures from Figure 4.8.
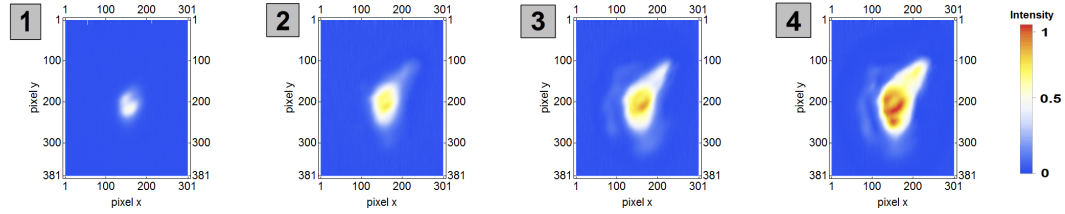
Figure 4.9: In-situ surface microscope - the insets refer to the same experiment like in Figure 4.8 and are background corrected as well as scaled identical.

Surface microscope can not differentiate from deposition and ablation. It recognizes only a change of the optics reflectivity. From the time resolved point of view it can be said, that the deposition process has to be before the ablation process, because LIC experiments operates at much lower fluence than the damage threshold. Nevertheless, it have to be considered, that the deposition process and the beginning of the ablation process could be within an image cycle (one cycle lasts around 50 sec). For this reason a low fluence is favourable for deposition time resolved investigations.

A more quantitative analysis of the in-situ microscopy is the integration of the signal intensity over a region of interest. The integrated signal intensity can be compared during the measurement as well as between different experiments. Integrated ROI for the above mentioned contamination experiment is plotted in Figure 4.10. Both graphs saturates after 25 minutes, what is in agreement of the in-situ transmission. The constant of the surface microscope signal indicates, that the surface morphology does not change anymore in a significant way. All in all the in-situ investigations have shown a high transmission degradation. Afterwards, the irradiated spots can be investigated by various kinds of microscopes like differential interference contrast microscopy (also known as Nomarski), ex-situ fluorescence, white light inference microscopy (WLIM) for the investigation of the z-Profile and scanning electron microscopy (SEM) in combination with an energy dispersive X-ray spectroscopy (EDX) for high magnification analysis and determination of the element distribution.

Nomarski microscope of the contamination experiment is shown for the beam entrance and exit face in Figure 4.11. The dark area of the images indicates
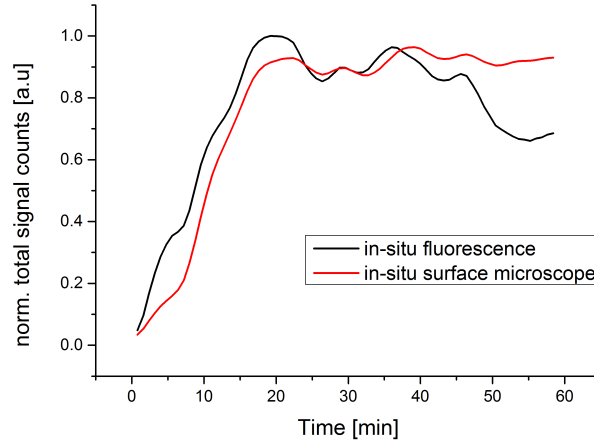
Figure 4.10: Normalized total counts of in-situ fluorescence and in-situ surface microscopy corresponding to the insets of Figure 4.8 and 4.9.

the damage area, where the surface of the coating was ablated. Spot characteristic of the ablated area is similar between the Nomarski and the in-situ surface microscope. The damage area is not an ideal circle, what can arise from the non-perfect beam profile and/or from a back reflection. The entrance and exit face have also different damage formation what has been discussed in the theoretical chapter.

(a) entrance face   (b) exit face
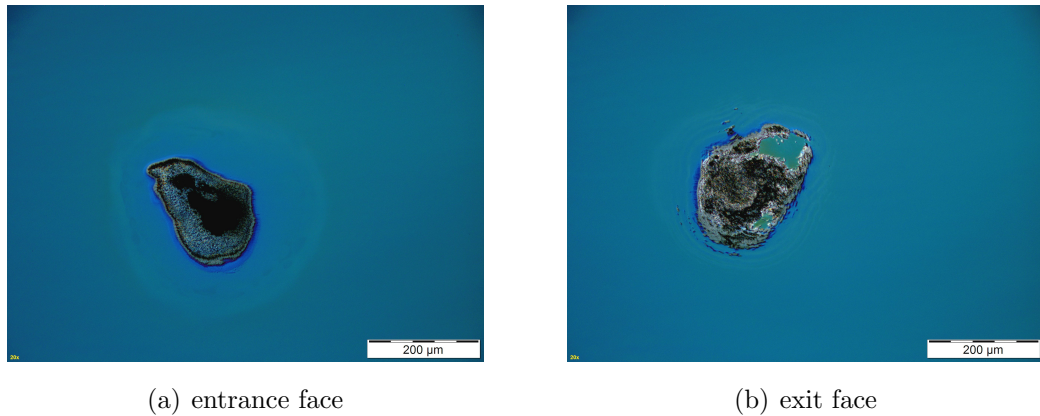
Figure 4.11: Ex-situ DIC of irradiated area with the fluence $1\,\mathrm{J/cm^2}$ and naphthalene atmosphere $10^{-5}\,\mathrm{mbar}$.

SEM and EDX microscope was used for the determination of the carbon dis-
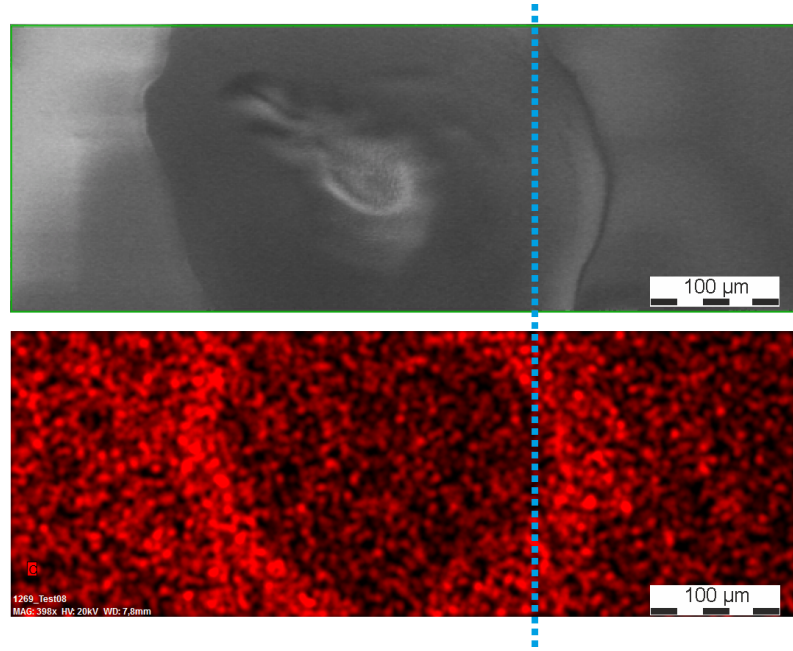
Figure 4.12: SEM-EDX investigation of the contamination experiment (fluence
1 J/cm^2 and naphthalene pressure 10^{-5} mbar) on the entrance side.
Upper row - the map selection of the SEM and lower row - carbon
distribution shows a doughnut-like profile determined by EDX.

tribution. The ablation process vanished the surface coating within the the
laser beam. The upper image of Figure 4.12 shows the investigation map of
the EDX, which corresponds to the same position as in Figure 4.11(a). Lower
image of Figure 4.12 refers to the distribution of the carbon concentration.
Higher carbon concentrations were found on the edge of the irradiated area.
The high fluence area with ablation phenomena shows no laser enhanced car-
bon concentration. The adsorbed contamination within this area is probably
ablated within a short irradiation time, due to the high surface temperature.
Another possibility is, that the surface temperature is too high and no con-
taminant adsorption can take place. This doughnut-like profile is in good
agreement with the stationary contamination experiment. By WLIM it was
determined, that surface was ablated up to $2 \, \mu$m. Optical coating layers are
partially or even completely ablated and the functionality of this optical coat-
ing can not be fulfilled anymore.

As a next step for preventing damage occurrence oxygen will be filled in the
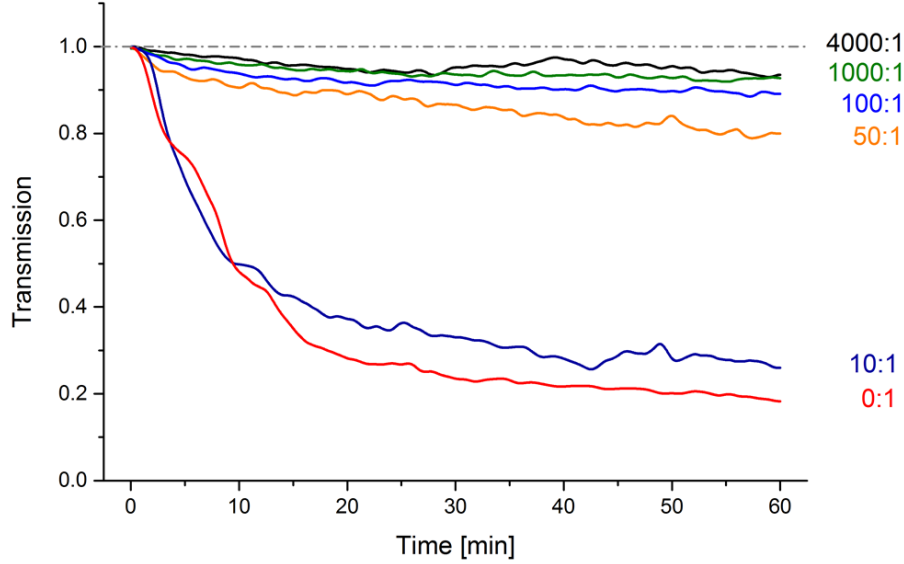
Figure 4.13: Experimental series of the fluence $1 \, \text{J/cm}^2$ and various oxygen -
naphthalene ratios. Absolute naphthalene pressure was $10^{-5} \, \text{mbar}$.
Ratio 0:1 and 10:1 shows ex-situ strong ablation. Break between
10:1 and 50:1 is obvious, but 50:1 experiment shows still ablation.
Higher ratios show in-situ and ex-situ only deposition.

test chamber for generating an oxygen - naphthalene atmosphere. The dynamical measurement procedure was introduced in *section 3.1* and will be followed for all the tests under the oxygen series. Adjusted concentrations were tracked in-situ during the whole irradiation time and were in all cases constant. In-situ transmission of the series with the fluence of $1.0 \, \text{J/cm}^2$ and the partial pressure of naphthalene of $1 \cdot 10^{-5} \, \text{mbar}$ is shown in Figure 4.13. The transmission behavior was measured with magnetron sputtered antireflective coating. E-beam coating as well as fused silica behave similar and are not shown in this section. The final transmissions values are summarized in the appendix.

Transmission lines over time reveal a break between the ratio 10:1 and 50:1 what is a strong indication for a threshold oxygen - naphthalene ratio. The transmission for the high ratios (4000:1 and 1000:1) have an identical transmission value after 3.6M pulses. Keep in mind, that the energy detectors are not temperature corrected and a small variation of the lab temperature influences the detectors sensitivity. In-situ fluorescence shows low intensity during high
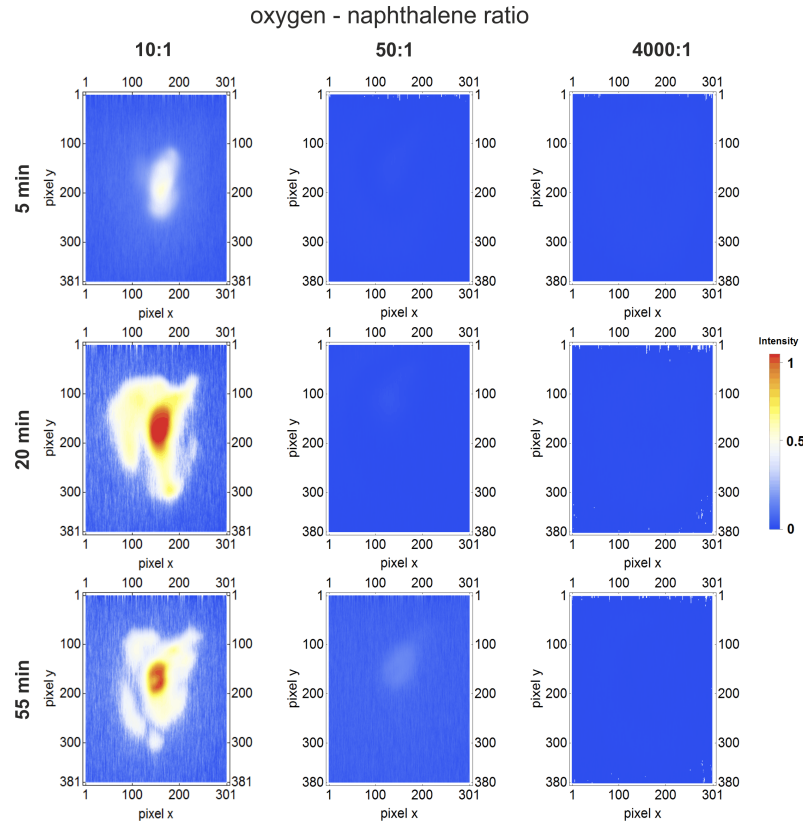
Figure 4.14: Comparison of in-situ fluorescence of the oxygen - naphthalene ratios 10:1, 50:1 and 4000:1 corresponding to experimental series of Figure 4.13.

oxygen ratios and the evolution of the in-situ fluorescence in dependence to the oxygen - naphthalene ratio is shown in Figure 4.14 between 10:1, 50:1 and 4000:1. The first column (10:1) shows still strong damage behaviour, reflecting the transmission curve and there is no obvious difference to the non-oxygen contamination test. The second column with the ratio of 50:1 shows within the first minutes very low fluorescence intensity, but the fluorescence increases with time and is not neglectable after 20 minutes. The third column has no visible fluorescence signal respecting to the scale. For this reason, it has to be analyzed more quantitatively and also the comparison to a blank test was performed. The comparison of the in-situ fluorescence between the blank experiment and the 4000:1 experiment showed no difference in the intensity.

In-situ surface microscopy shows a very small signal change indicating a small
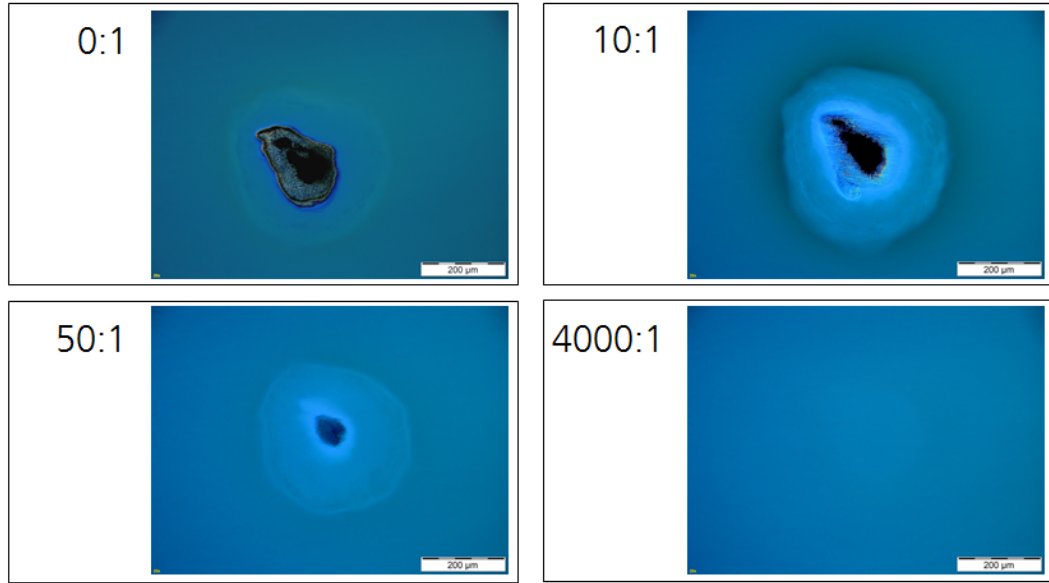
Figure 4.15: Ex-situ DIC of the entrance face corresponding to experimental series of Figure 4.13. Evolution of the increasing oxygen influence to higher oxygen - naphthalene ratios.

deposition layer of contamination, which have to be clarified ex-situ.

Nomarski images in Figure 4.15 of the entrance side, corresponding to the transmission tests shown in Figure 4.13, give a good impression of the evolution from low oxygen - naphthalene ratio to higher ratios.   Only ex-situ
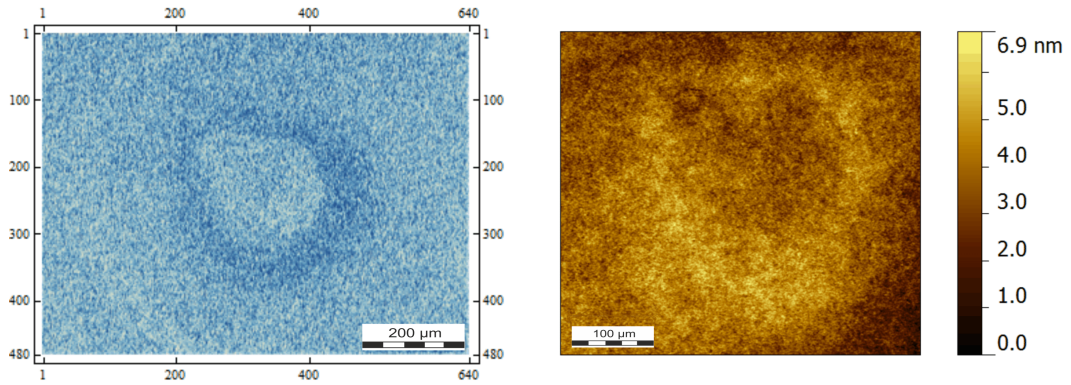
Figure 4.16: lhs: background corrected ex-situ DIC of the entrance side of the 4000:1 experiment.   Small deposition is visible rhs: deposition profile was quantified by the WLIM - higher deposition at lower fluence area.

investigation of the 4000:1 experiment is present, what represents the best performance considering the transmission. Differential interference contrast measurement has to be background corrected to visualize the irradiated area (Figure 4.16 (a)), what is in good agreement to the in-situ surface microscope. The disturbance by the laser irradiation is very small. WLIM signal indicates also a small deposition layer (see Figure 4.16 (b)) in the nanometer range. The deposition of contamination material is very low but it can not be prevented completely.

The transmission behavior of the irradiated samples under different oxygen - contamination ratios determined a positive effect with increasing ratios. Transmission values of the experimental series from Figure 4.13 is plotted versus the ratio in Figure 4.17 It is obvious, that the breakpoint of the ratio is described
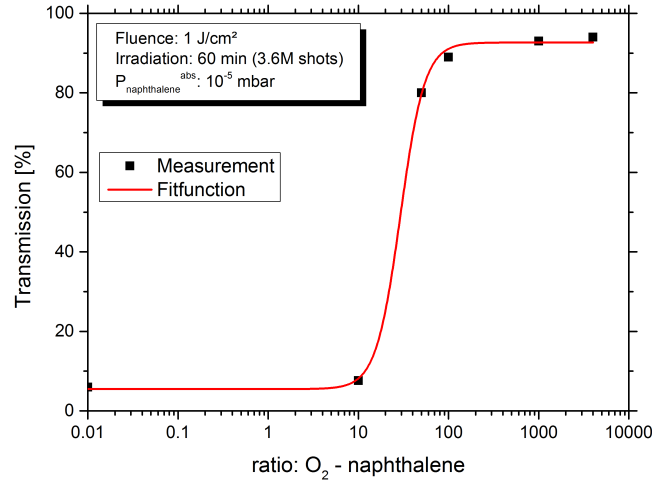
Figure 4.17: Transmission values after irradiation for different oxygen - naphthalene ratios corresponding to experimental series of Figure 4.13. Fitfunction of the growth model determined a breakpoint ratio.

between 10:1 and 50:1. This breakpoint was confirmed over different laser fluence and even a higher partial pressure of naphthalene. Lower fluences than $1\,J/cm^2$ were not discussed, because the results of $1\,J/cm^2$ are for satellite systems critical. But the confirmation, that the limit ratio is also valid for lower fluences as well as higher contamination pressure increases the confidence level

of the method. In the appendix results are shown for a higher absolute contamination pressure and for the laser fluences $0.3\,\mathrm{J/cm^2}$, $0.6\,\mathrm{J/cm^2}$ and $1.0\,\mathrm{J/cm^2}$. The fitfunction is given by the following formula:

$$f(x) = A + \frac{B - A}{1 + \left(\frac{x}{x_t}\right)^2} \tag{4.1}$$

Variables A and B define the lowest and highest level of the transmission. Whereas x_t is the breakpoint and corresponds to the average of A and B. The breakpoint x_t can be corresponded to a threshold ratio. But for the prevention of ablation, the ratio should be higher than the breakpoint. Nevertheless, the breakpoint pictures the turnover very well and indicates a starting prevention mechanism. This formula is often used for challenges with a threshold point and is categorized into the so called growth model [45], [46], [47].

With the knowledge of the positive oxygen effect, a long term experiment over $6\,\mathrm{h}$ and $21.6\,\mathrm{M}$ pulses was performed and characterized. Transmission curves are shown in Figure 4.18 on the left hand side. The right hand side shows the
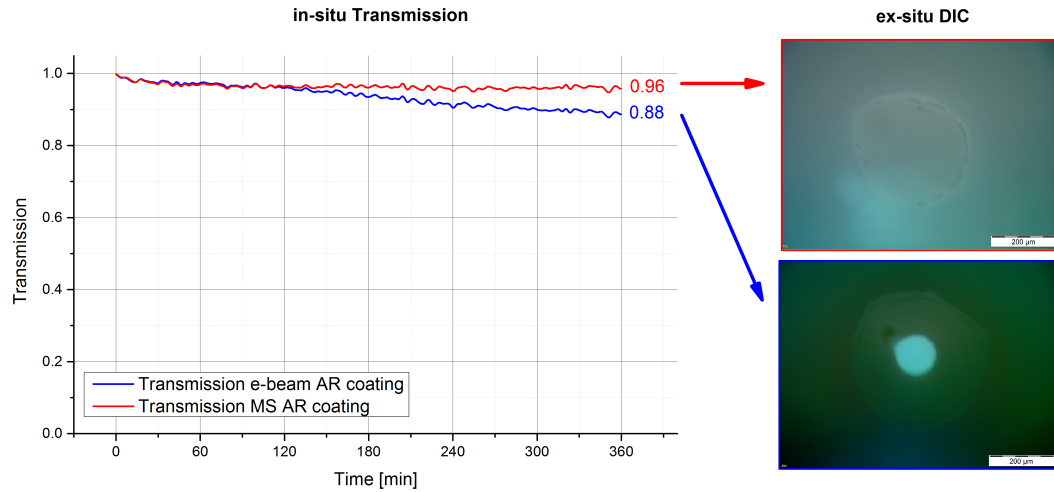
Figure 4.18: Longterm test under oxygen - naphthalene 4000:1 atmosphere with the fluence $1\,\mathrm{J/cm^2}$ and a absolute naphthalene pressure of $10^{-5}\,\mathrm{mbar}$. lhs: transmission over time for MS and e-beam AR coating rhs: ex-situ DIC of the entrance face - ablation phenomena at the e-beam sample visible.
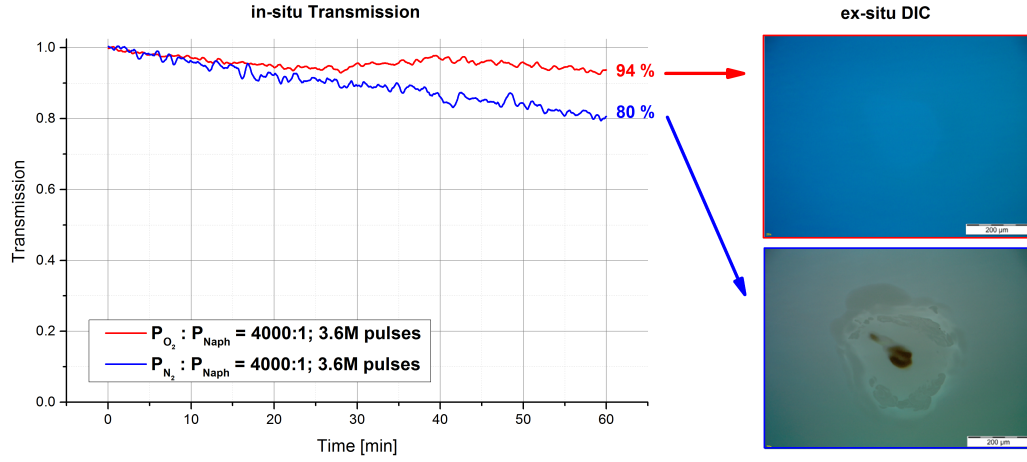
Figure 4.19: Comparison between an oxygen - naphthalene 4000:1 and nitrogen - naphthalene 4000:1 atmosphere irradiation with the fluence $1\,\mathrm{J/cm^2}$ and a absolute naphthalene pressure of $10^{-5}\,\mathrm{mbar}$. LHS: transmission over time for a MS AR coating. RHS: ex-situ DIC of the entrance face - ablation phenomena for the nitrogen experiment visible.

Nomarski images of the entrance face for the coatings - magnetron sputtered and e-beam antireflective coating. Transmission line is for both samples similar till 120 minutes of irradiation and splits then. The e-beam coating degrades to 88 % - a non neglectable transmission loss. Nomarski indicates ablation phenomena within the high fluence region of the e-beam coating, whereas the surface of the MS coating shows deposition traces without visible ablation. WLIM quantified the ablation of the e-beam coating to $30\,\mathrm{nm}$ and in contrast has the MS coating a deposition of around $5\,\mathrm{nm}$ thickness. This is comparable with the 60 minutes test of the same parameter constellation. The e-beam coating can not withstand the long irradiation compared to the MS coating. An IBS antireflective coating was also tested and shows the same behavior like the MS coating. The sputtering coating technique is for this experimental configuration the better one.

 After the influence of oxygen could be investigated successfully, the question is, whether other gases like nitrogen can imitate the effect. So, optics were irradiated under nitrogen - naphthalene 4000:1 atmosphere. Also nitrogen

exhibit a positive effect, but only in the way, that the fast damage formation under contamination atmosphere will be delayed. The transmission curve of Figure 4.19 in direct comparison to the oxygen test exposes higher transmission loss down to 80 %. Ex-situ DIC on the rhs of Figure 4.19 indicates for the nitrogen test ablation phenomena on the MS, e-beam and IBS sample. The WLIM confirmed the ablation process for all coating types.

4.1.3 LIC-Deposition and cleaning procedure

In this part, a deposition of contamination and a following cleaning sequence will be described. The sensitivity of the long distance microscope is essential for the online recognition. To avoid damage formation, the fluence was reduced to 0.1 J/cm^2. Absolute naphthalene pressure was in the range of $1 \cdot 10^{-5}$ mbar and no oxygen was inserted for the formation of the LIC-Deposition.

Naphthalene pressure was kept constant during the deposition. Shortly after the irradiation was started, the formation of the LIC-Deposition was visible in-situ via the long distance microscope. The LIC formation is shown in the image series of Figure 4.20. On the upper row, the in-situ images of the surface microscope is shown and on the lower the in-situ images of the fluorescence with similar time stamps. The red cross has the same position in both images to localize the spot. Moreover it has to be respected, that the in-situ surface microscope can not differentiate between deposition and ablation. For ex-situ characterization of the deposition spot, a second experiment was performed under identical parameters. This is necessary, because the test sample could not be removed after the LIC formation and inserted again on the exact same position.

Consequently, the second experiment was performed under the same conditions and an similar LIC-Deposition was identified in-situ. In-situ microscope determined the dimension of the LIC-Deposition to 10 μm, what could be confirmed by ex-situ microscopy and the WLIM reveals a height in the region of 50 nm. Element analysis of the spot by EDX revealed a significant concentration of carbon. Corresponding spectra from the LIC spot and from an
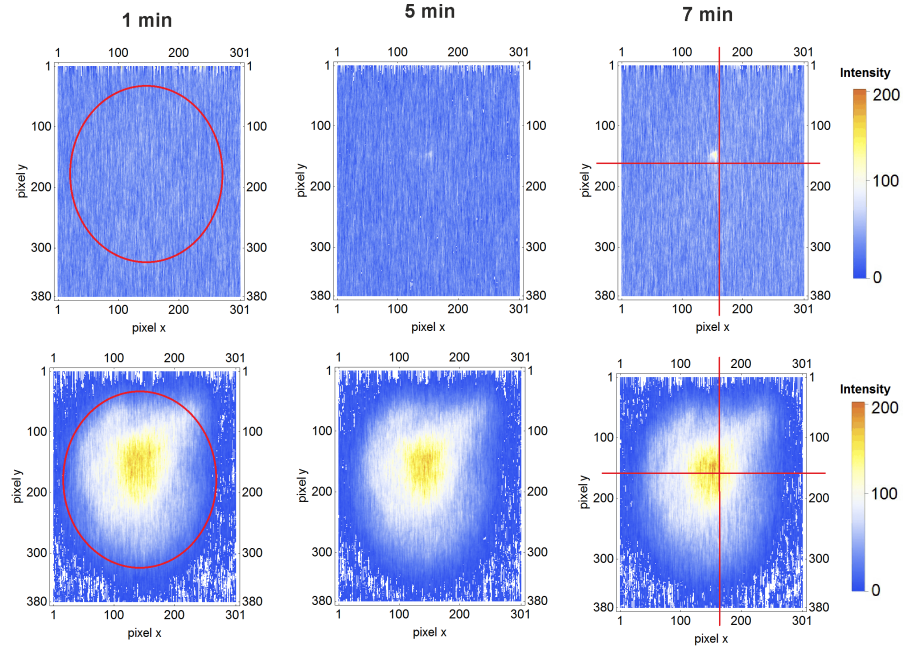
Figure 4.20: In-situ microscope images of the LIC formation. Upper row shows the surface microscope and the lower row shows the fluorescence microscope images. Red circle indicates the irradiation area and the red cross is placed identical to indicate the LIC spot.

unirradiated surface is shown in Figure 4.21.

The spectra are obviously different and a carbon peak is not visible for the unirradiated surface. A quantification of the X-ray spectra for the determination of the element concentration has to be performed. This is done by the ZAF method, which correlates the atomic mass, the cross section and fluorescing mechanism of the elements. For more information is the lecture from Dr. Chatterjee is recommended [48]. The quantified element concentrations deliver the following element composition - Table 4.3

Element	$C_{\text{LIC-Spot}}$ [At %]	$C_{\text{unirradiated surface}}$ [At %]
Carbon	59.6	-
Oxygen	32.4	65.4
Silicon	8.0	34.6

Table 4.3: Quantified element concentration of the LIC spot and an unirradiated surface.

(a) Unirradiated surface
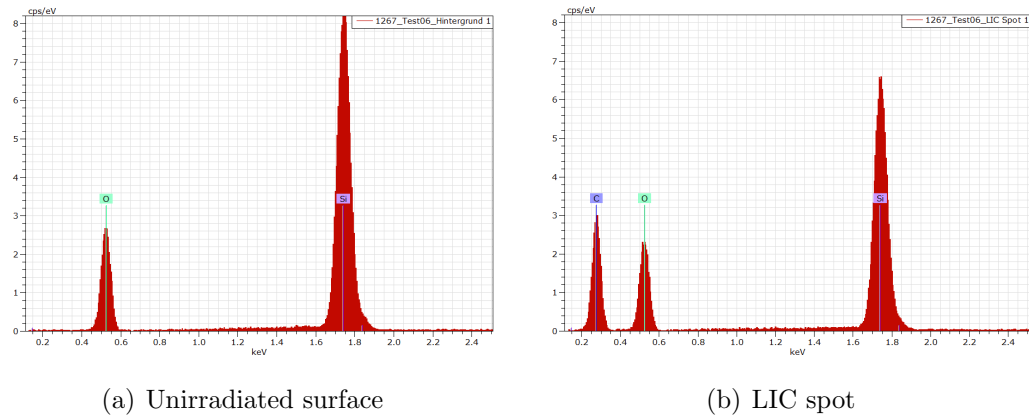
(b) LIC spot

Figure 4.21: Comparison of the EDX spectra from the LIC spot and an unir-
radiated surface. Acceleration voltage of 20 keV and the variable
pressure mode was used.

The generation of LIC-Deposition with low fluences works well and delivers
high concentration of carbon within the spot size. Now, a proof of concept
for the LIC-Deposition cleaning is presented. Naphthalene was pumped out to
reduce the partial pressure of contamination below 10^{-6} mbar and a pressure
of 40 Pa oxygen was inserted to the chamber. In-situ microscope traced the
cleaning procedure and after 5 min of irradiation with the same fluence like the
LIC-Deposition formation. The intensity of the surface microscope and the flu-
orescence signal on the located spot decreased to blank test level. Within the
cleaning procedure, the fluorescence camera signal increased temporary and
indicates the activated reaction between the contaminants and the oxygen.
The formation and cleaning procedure was repeated on the same spot with
10 Pa and 2 Pa oxygen and the LIC-Deposition spot could be vanished every
time (shown on the rhs of Figure 4.22). But it has to be taken into account,
that during the cleaning process, no naphthalene was inside the chamber.

To get more confidential evidence of the cleaned surface ex-situ inspection
has to be taken into account. Neither DIC, WLIM nor the high magnification
SEM showed any deposition on the irradiated surface. These aspects support
the in-situ investigations of the cleaned surface by the irradiation under oxy-
gen atmosphere.
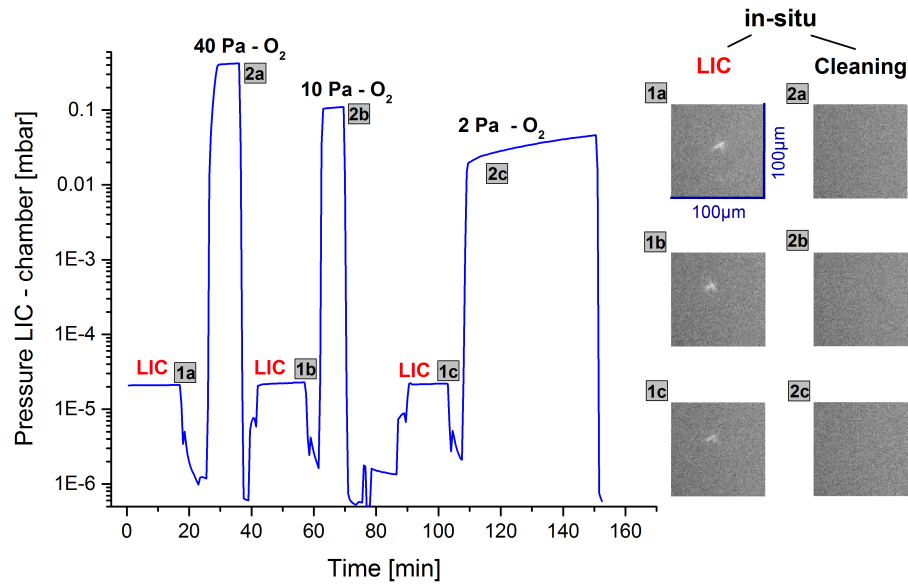
Figure 4.22: LIC-Deposition and cleaning sequence with the fluence $0.1\,\mathrm{J/cm^2}$
lhs: absolute   pressure   within   the   science   cham-
ber   during   LIC-Deposition   and   cleaning   sequence
rhs: in-situ   surface   microscope - the   left   insets   correspond   to
the   LIC-Deposition   and   the   right   one   to   the   cleaned   surface.
The   cleaned   areas   shows   no   differentiation   to   the   area   before
irradiation.

4.1.4   Influence of Au-nanoparticle inclusions on AR coatings

The production process of optical coatings, especially for multi layer coatings,
is highly dependent on the interface purity. Particle inclusions could increase
the optical absorption immensively and should be avoided entirely.
In coorperation with the Laserzentrum Hannover (LZH) antireflective coatings

NP concentration	Absorption [%]
no	0.23
low	0.57
high	1.02

Table 4.4: Absorption difference of the nanoparticle samples.
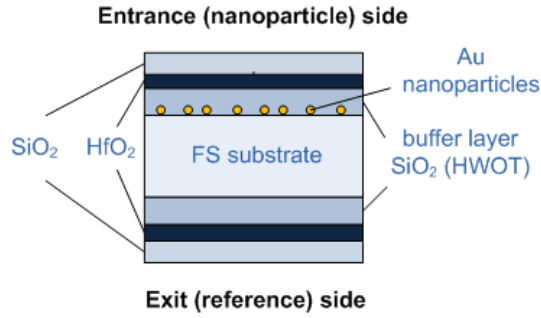
Figure 4.23: Layer compositionm of gold nanoparticle optics.

were produced with an interface layer containing gold nanoparticle. A sample series with different artificial particle concentrations were produced: a high particle concentration sample, a low one and one without artificial nanoparticles. All three of them are produced under the same coating procedure, what is essential for their comparison. The optic's layer composition is sketched in Figure 4.23. Absorption of the three coatings was measured at 355 nm with an average power of 0.86 W (see Table 4.4)

The samples were irradiated in the preface with the fluence of $800\,\text{mJ/cm}^2$ without any contaminants to check the coating stability. No transmission loss or damage formation was recognized - neither in-situ nor ex-situ. All the following contamination tests were performed under dynamic contamination atmosphere with an absolute naphthalene pressure of $1 \cdot 10^{-5}\,\text{mbar}$. Already

(a) 60 min

(b) 120 min
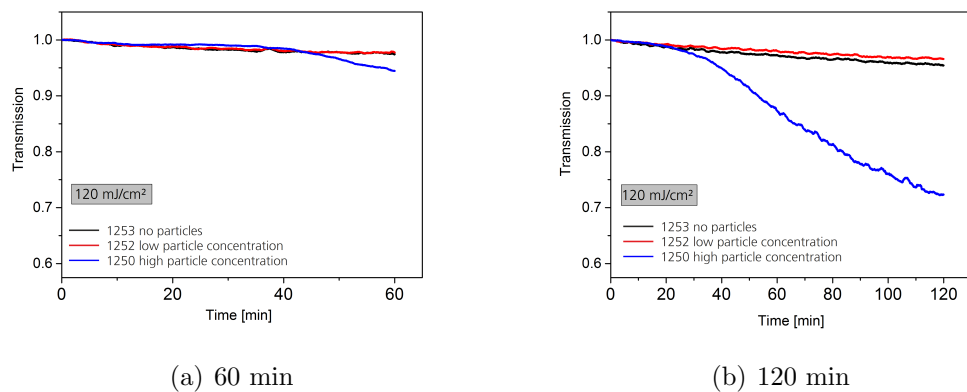
Figure 4.24: Irradiation of gold nanoparticle samples with a low fluence of 120 mJ/cm^2.
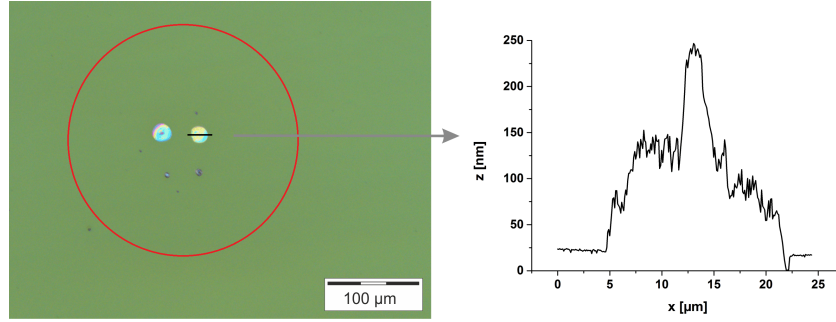
Figure 4.25: High concentration Au-nanoparticle sample after 60 minutes irradiation with $120\,\text{mJ/cm}^2$ at naphthalene pressure of $10^{-5}\,\text{mbar}$.

a low fluence of $120\,\text{mJ/cm}^2$ affects the transmission over irradiation time of 60 min and 120 min of the high particle concentrated sample. Low concentration and reference sample are barely influenced by the irradiation and behave very similar (see Figure 4.24).

In-situ transmission line over time of the 120 min test is the continuation of the 60 min test. Ex-situ investigation of the spots shows for the 60 min test microspots on the Nomarski and the AFM exhibited pancake-like deposition (Figure 4.25). For the 120 min test the Nomarski shows a larger spot in the high fluence region and a doughnut-like profile was measured by the WLIM (Figure 4.26). Transition from pancake to doughnut structure is well known for LIC growth [8]. EDX analysis confirms the carbonaceous nature of the pancake deposition and on the edge of the doughnut profile [49]. Deposition starts obviously in the high fluence region of the Gaussian beam profile on small spots, which seems randomly distributed. Because the nanoparticles are
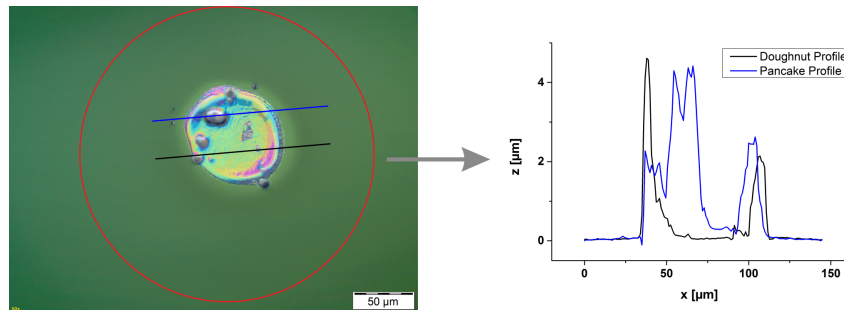
Figure 4.26: High concentration Au-nanoparticle sample after 120 minutes irradiation with $120\,\text{mJ/cm}^2$ at naphthalene pressure of $10^{-5}\,\text{mbar}$.
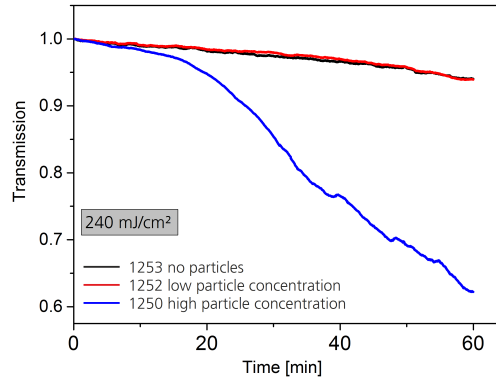
Figure 4.27: Transmission of Au-nanoparticle samples under 60 minutes irradi-
ation with $240\,\text{mJ/cm}^2$ at naphthalene pressure of 10^{-5} mbar.

distributed homogeneously with a spacing of about few tens of nanometers, it
is very unkind that the nanoparticles are the seeds of deposition spots them-
selves. Nevertheless the effect of the nanoparticle concentration is evidently,
because the two other samples do not show a strong influence by the laser
induced contamination. Probably after the formation of many carbonaceous
spots, they will overlap and form a larger spot with an overall profile of a
doughnut including small pancake like profiles of deposited carbon. On the
back side, which has no artificial nanoparticle at all, there was no sign of de-
position structures, what is another indication of the nanoparticle influence.

The last test of these series without oxygen was performed with a higher
fluence of $240\,\text{mJ/cm}^2$, what is still far less than the blank test fluence of
$800\,\text{mJ/cm}^2$, which showed no degradation signs. In-situ transmission of the
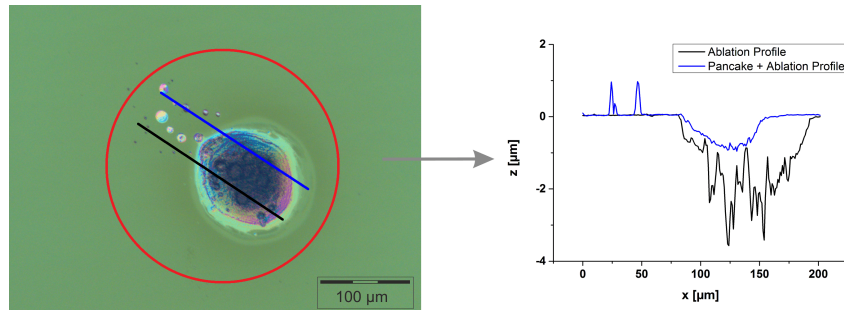
Figure 4.28: High concentration Au-nanoparticle sample after 60 minutes irra-
diation with $240\,\text{mJ/cm}^2$ at naphthalene pressure of 10^{-5} mbar.
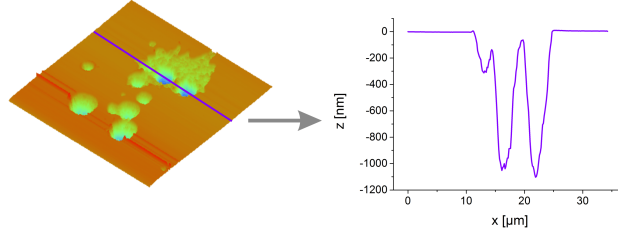
Figure 4.29: AFM of the exit face shows crack formations (lhs) with depths
up to one micrometer (rhs) after irradiation with the fluence of
$240\,\text{mJ/cm}^2$.

high particle sample started to degrade after 20 min or 1.2M pulses. After an-
other 40 min or 2.4M pulses the transmission degraded to 62 % (Figure 4.27).
Low particle and reference sample behaved similar again and just degraded to
94 %. Also no deposition or ablation was found on the entrance side of the
low particle and reference sample. The corresponding ex-situ DIC and WLIM
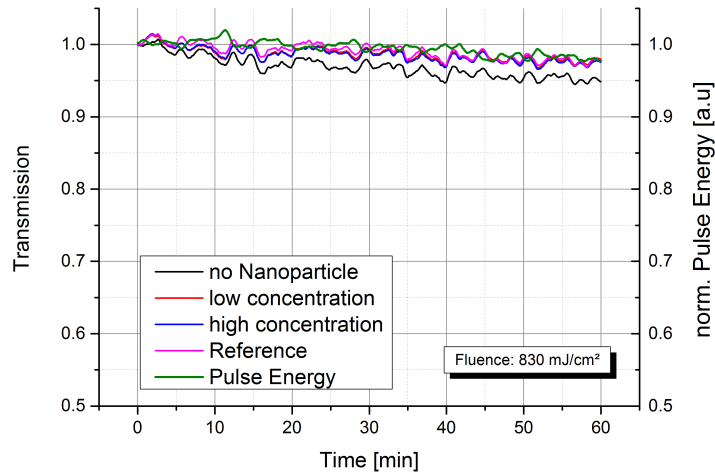
Figure 4.30: Transmission over time of Au-nanoparticle samples under 60 min-
utes irradiation with $830\,\text{mJ/cm}^2$ under the oxygen - naphtha-
lene ratio of 4000:1 and with an absolute naphthalene pressure of
$10^{-5}\,\text{mbar}$.

investigation of the high nanoparticle sample is shown in Figure 4.28. White light interference microscopy shows in the center of the laser beam ablation of the surface up to 3.5 μm and in the region of medium fluence pancake like carbon spots were formed up to 3.5 μm. Moreover the EDX analysis shows a significant amount of incorporated carbon within the ablation spot, although there was no deposition growth formation found. In contrast to the irradiation with a fluence of $120\,\text{mJ/cm}^2$, the exit face of the samples shows ablation signatures with depth of around one micrometer (see Figure 4.29). Exit face ablation phenomena was already discussed in former work with equivalent fluences [28] [50]. Moreover the laser damage threshold is at least one magnitude higher for those samples in a non-contaminated atmosphere.

The positive influence of an oxygen atmosphere will be presented here as well, but only for the oxygen - naphthalene ratio of 4000:1. Samples were irradiated with the same fluence like the contamination tests without oxygen and also at a fluence of $830\,\text{mJ/cm}^2$. Figure 4.30 shows the transmission behaviour. Significant influence of the oxygen atmosphere is obvious compared to Figure 4.24 and Figure 4.27.

During the irradiation of the samples with the oxygen - naphthalene atmo-

(a) whole beam   (b) beam center
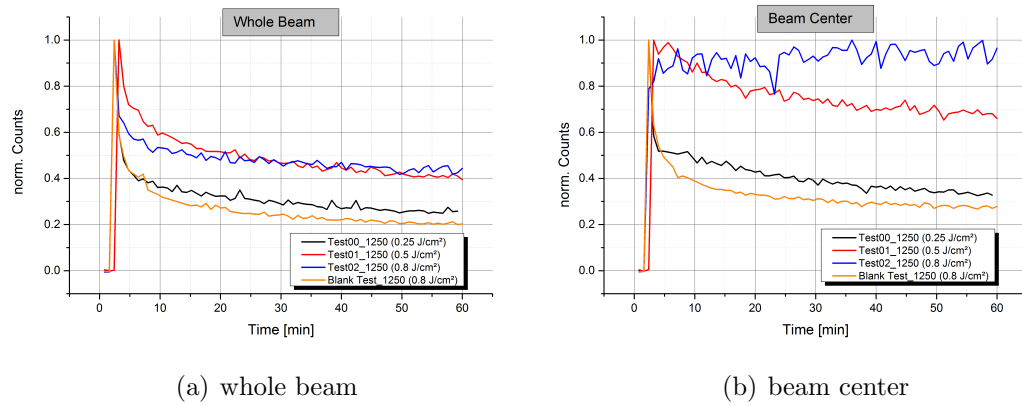
Figure 4.31: Comparison of the normalized in-situ fluorescence signal in dependence of the beam area. LHS: Normalized count rate over time of the whole laser beam for various fluences. Count rate shows usual behavior. RHS: Normalized count rate over time of the center of the laser beam for various fluences. Count rate differentiates between each other, normalization should bring them together. Probably another effect influences the camera signal.

sphere was an unusual behavior of the intensity distribution with the fluorescence camera detected. The signal shows an highly increased intensity in the beam center with increasing fluence on the sample with high Au-nanoparticle concentration (see Figure 4.31). This was not seen in former experiments. Mostly the experiments showed an increased signal corresponding to the Gaussian shape. But here the quantity of the increased signal can not completely correlated to the peak function. The origin is unknown till now and should be investigated in future work.

4.2 LIC experiments with spaceborne contaminants

All the tests above were performed with naphthalene, a molecule with a high vapor pressure and quite easily manageable for defined contamination pressures. The challenge of testing spaceborne contaminants is the varying outgassing rate, due to the fact, that volatile elements as well as molecules are pumped up and to hold a constant contamination pressure is not for sure. For this reason, the contamination chamber is heated, to extract even bounded molecules in the view, to get a high reservoir of possible contamination molecules. Nevertheless, the possibility of an infinite contamination reservoir will not be reached like for the naphthalene case.

For the following case, the extraction of araldite [51] as well as for solithane [52] was positive, what means a constant contamination pressure of 10^{-5} mbar for several hours was reached and also deposition at irradiated spots could be induced. But take also into account for further statements, that in working satellite systems the contamination pressure is at least one magnitude lower. Because solithane was easier to manage the outgassing rate, the shown tests below refers to the contamination material solithane. Solithane is a polyurethan and is used for screw lockings and conductive coatings [52].
Moreover, all the tests in the following section were performed with the fluence $1 \, \text{J/cm}^2$ and a repetition rate of $1 \, \text{kHz}$.

4.2.1   Solithane as a spaceborne contaminant

Pieces of solithane coated foil were inserted to the contamination chamber and the contamination chamber was pumped to UHV region. Afterwards the chamber was heated up to 100°C . The pressure increased in the LIC chamber as well as in the differential pumped RGA chamber and the RGA system recognized increasing peaks for the atomic masses of 44, 28, 26 and 12. The peak of 44 and 28 is characteristic for carbon-dioxide and nitrogen, but the chambers were pumped up completely to ultra high vacuum and the increasing of the peaks refers to an outgassing of carbon-molecules, for example the atomic mass 28 correspond to ethen (C_2H_4). With a total pressure in the LIC chamber of 10^{-5} mbar and significant peaks with the above mentioned atomic masses in the RGA spectra, the irradiation of the optics was started and lasted for 120 min respecting 7.2M pulses. In-situ LDM surface-microscopy measured a change of the intensity distribution. The in-situ fluorescence showed also increased activity and the combination of both microscopes indicate the deposition of contamination on the surface. Ex-situ DIC measurement (Figure 4.32) shows a deposition layer.

The next steps are to show the positive effect of oxygen in two ways. One is the creation of an oxygen - solithane atmosphere with a high ratio of oxygen
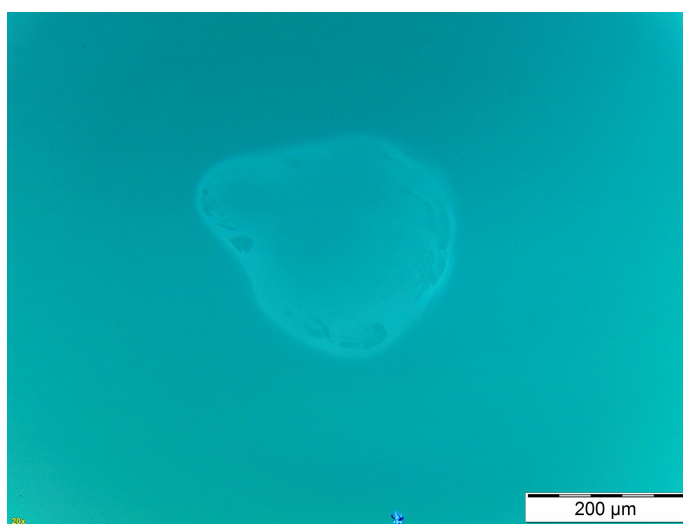
Figure 4.32: Ex-situ DIC of the entrance face shows deposition phenomena after the irradiation for 2 h with the fluence $1 \, J/cm^2$ and a contamination pressure of 10^{-5} mbar.
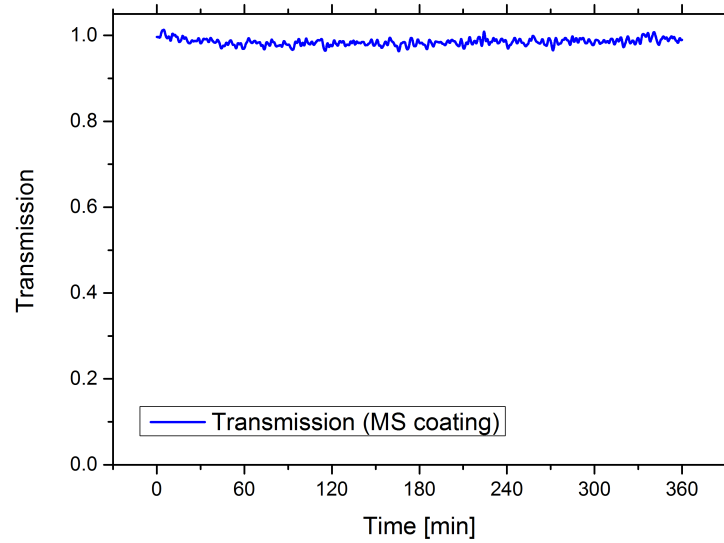
Figure 4.33: Transmission over time during the irradiation with the fluence
$1\,\mathrm{J/cm^2}$ under $40\,\mathrm{Pa}$ oxygen atmosphere and dynamic pumped con-
tamination pressure of $10^{-5}\,\mathrm{mbar}$ shows no transmission degrada-
tion after $6\,\mathrm{h}$, respectively $21.6\,\mathrm{M}$ pulses.

compared to solithane. The other one is the deposition of contamination and
the cleaning afterwards with the insertion of oxygen, but in this case, the con-
tamination elements will remain in the chamber.

The Aladin laser of ADM-Aeolus will be sealed and pressurized with $40\,\mathrm{Pa}$
oxygen. Consequently the tests will be performed with similar pressure. The
challenge is, that the contamination concentration could not be monitored in-
situ. Following steps were done, the contamination was inserted, than the
$40\,\mathrm{Pa}$ of oxygen was added and the irradiation will start, still under dynamical
pumped, so the partial pressure of oxygen and solithane remains in a constant
regime. Afterwards the oxygen is pumped up to get ride of them and the
contamination pressure remains in the LIC chamber. Then another test was
run with this contamination pressure, to be sure, that the contamination is
still within the chamber. So, at first a oxygen - contamination atmosphere
was created and the optics were irradiated for 6h respectively 21.6M pulses.
In-situ transmission (Figure 4.33) remains nearly constant over the whole time
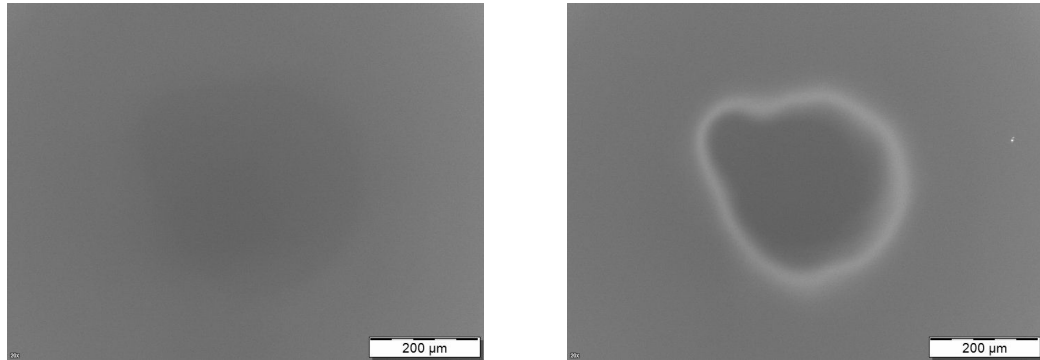
(a) longterm experiment under oxygen - solithane atmosphere

(b) deposition effect of solithane

Figure 4.34: (a) Ex-situ fluorescence after the longterm experiment from Figure 4.33 shows no sign of deposition or even ablation. (b) Ex-situ fluorescence of a deposition test directly performed after the longterm experiment to prove the contamination pressure. Deposition on the edge of the irradiation area is obvious.

region of irradiation, what is quite favorable.

In-situ fluorescence as well as surface microscope show no deposition effects at all. Ex-situ Nomarski exhibit no disturbance of the irradiated surface. The ex-situ fluorescence (Figure 4.34 (a)) is only very weak and similar to blank tests. Oxygen pressure prevents reliable the formation of deposition. Because the experiments are performed sequentialy, the whole sample exhibit a low concentration of adsorbed contamination molecules on the optics surface which are visible on the ex-situ fluorescence.

Scanning electron microscopy was performed with high magnification on a non-irradiated area as a reference (Figure 4.35(a)) measurement of the surface. Surface is not perfectly smooth and exhibits very small defects. The comparison of the irradiated surface to the non-irradiated surface shows no visible difference considering laser induced contamination (Figure 4.35(b)). No micro-cracks were found and the surface characteristic is similar to the reference area.

Directly after the longterm experiment a deposition test without oxygen was started, to prove the existence of contamination material within the LIC cham-

(a) non-irradiated area

(b) high fluence region of longterm irradiation
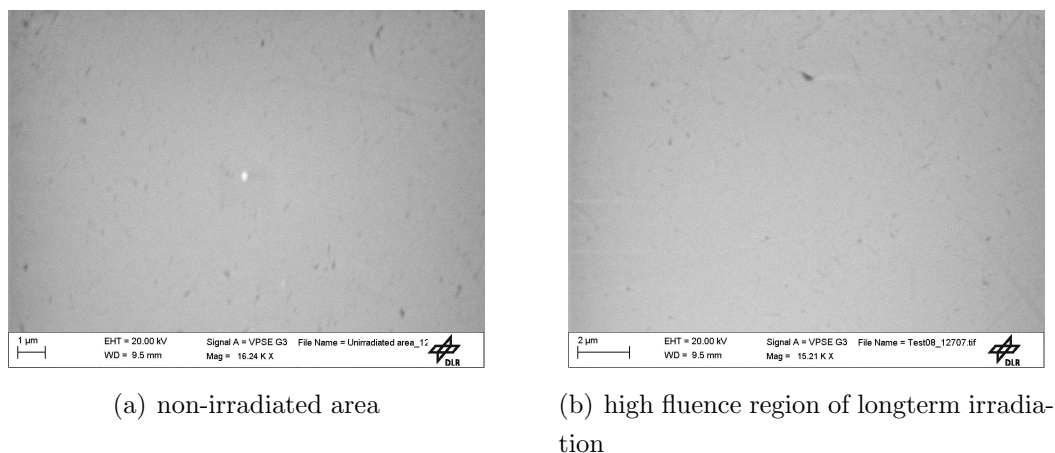
Figure 4.35: Comparison of high magnification between unirradiated and irradiated surface with SEM shows no crack formations or effects considering laser induced contamination.

ber. In-situ surface microscope noticed the laser induced depositing effect after 2M pulses. Ex-situ DIC shows deposition as well and the ex-sit fluorescence (see Figure 4.34(b)) has a strong intensity signal of the contamination. Consequently it can be concluded, that during the longterm test under oxygen atmosphere, a lot of contamination material was inside the chamber and the deposition due to laser induced contamination could be prevented. This deposition test shows equivalent behavior like the presented deposition test in Figure 4.32.

Laser supported cleaning under oxygen atmosphere of deposited contamination was tested as well. The origin of the contamination under naphthalene atmosphere was clear and the molecule composition is known for the deposited material. But due to the unknown molecule mixture of solithane, the cleaning process has to be performed under these conditions to show that any kind of carbon-molecules can be cleaned. After deposition was formed and detected via the in-situ microscopes, $40\,Pa$ oxygen were additionally inserted. Deposition process with a contamination pressure of $10^{-5}\,mbar$ took in comparison to the naphthalene much longer. Also the deposition structure was different. For the naphthalene contaminant discrete structures were detected, whereas for solithane deposition was formed at the lower fluence area of the laser beam

(like it was shown in Figure 4.32). It can be assumed, that LIC growth is stronger with naphthalene compared to solithane. The cleaning process took also 7.2 M pulses like for the deposition process. Nevertheless, the ex-situ Nomarski investigation showed very small deposition (see Figure 4.36 lhs). But the among of remaining deposition is much lower than without any cleaning. The remaining small deposition is in the region of low fluences respecting the
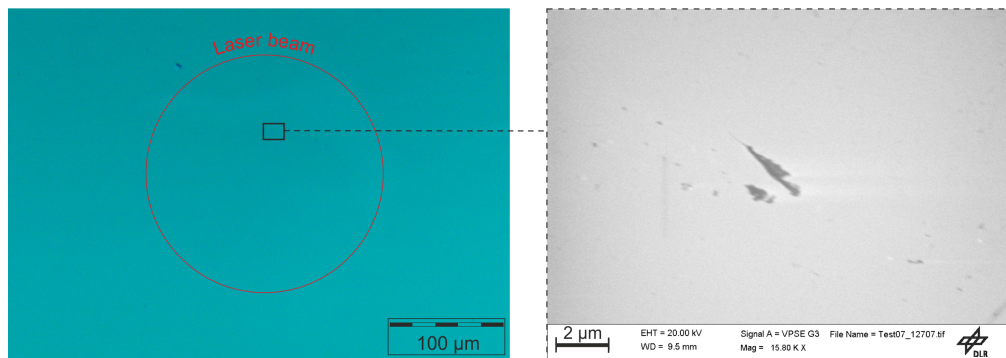
Figure 4.36: lhs: Nomarski   microscope   of   the   entrance   face   after   the   LIC-Deposition   and   cleaning   sequence. rhs: SEM shows small crack formations within the deposition area and are corresponded to contamination phenomena.

Gaussian intensity profile. This opens the assumption, that higher fluence is needed for cleaning deposited contamination. Probably, a more detailed investigation of the surface is needed to exhibit the surface mechanism due to the contamination. Nevertheless, most of the deposited contamination was cleaned what supports the cleaning mechanism. But with the high magnitude of the SEM crack formations within the irradiated area were found (see Figure 4.36 rhs). It is assumed, that the high fluence formed heated spots due to the deposited contamination. The cracks are connected to the deposition, because they were just found in the deposition area. This fact indicates, that the high fluence can disturb the surface even on small deposition. Cleaning process with oxygen atmosphere is probably not involved to the crack formation, because the longterm test (Figure 4.35) with equivalent pressure configuration does not show surface crack formations. Even though, there was no strong ablation and no transmission loss recognized on the LIC-Deposition and cleaning area. The irradiation with an oxygen - contamination atmosphere from the beginning of the experiment is preferred.

5 Conclusion and Outlook

5.1 Conclusion

The implementation of the differential pumped RGA system for the exploration of an unknown threshold ratio for the oxygen - contamination atmosphere was successful. A triggered in-situ fluorescence camera and an in-situ surface microscope enhanced the monitoring of contamination processes. Effects from the increasing oxygen - naphthalene ratio manifested a positive influence concerning the transmission behavior. The deposition of contamination can be suppressed to a very low level as well as no ablation processes are taking place under relevant fluences with a defined ratio larger than 1000:1. Achieved transmission values over the test series corresponding various fluences as well as for both contamination pressures showed a clear threshold ratio, even though the value of the threshold ratio is equivalent over the whole test range. Nevertheless, there is still a small transmission loss of around 5 %. This result is valid for the irradiation of magnetron sputtered and ion beam sputtered coatings for time durations of 60 minutes and 360 minutes. Magnetron sputtered and ion beam sputtered antireflective coating showed no difference between the short test and the longterm test. The e-beam coating shows also a transmission loss of 5 % for the 60 minutes test, but the irradiated surface of the longterm test showed ablation phenomena and the transmission decreased to 80 %. Consequently the magnetron sputtered and ion beam sputtered coatings have a higher resistivity against the contamination atmosphere than the e-beam coating. The test conditions were the same, because of the simultaneously irradiation. The small transmission loss arises the idea, that a small change of the surface layer will change the defined behavior of the coating

layers. The antireflective coating layers are manufactured in the way of destructive interference for 355 nm. A change of the refractive index between the vacuum and the first coating layer will change the destructive interference condition. In principle, a small deposition layer of contamination can change the refractive index due to the interaction of the electromagnetic wave of the laser beam and the small deposition layer of the molecules. The molecules will be polarized and influences the wave propagation. Moreover, the transmission loss occur within the first hour but it will remain constant for longer tests, what indicates no further transmission loss. Even there was an increased deposition visible, regarding to the Nomarski images of the MS coating (Figure 4.15 and Figure 4.18 rhs), the transmission loss stopped within the first hour of irradiation and it seems that the influence of the contamination saturated. All in all is the transmission performance in a highly reasonable region for a high ratio of the oxygen - naphthalene atmosphere, especially taking into account, that real system have at least on magnitude lower contamination pressures. The effect of nitrogen was also investigated, but the performance was worse compared to oxygen and also ablation process took place on the irradiation area of the nitrogen test.

The threshold ratio indicates a chemical prevention process and this fact was also used for the cleaning of a consciously deposited LIC formation. Contamination spots with the dimension of the micrometer regime were formed under low fluences ($100 \, \text{mJ/cm}^2$). The in-situ monitored spots could be cleaned by a laser induced cleaning under oxygen atmosphere. Further surface investigations have not revealed a disturbance of the irradiated surface due to the contamination and cleaning process. Moreover, the in-situ fluorescence measured an increased signal on the position of the contamination spot during the cleaning process, what indicates a laser induced chemical reaction.

A high purity of coatings is necessary for laser applications and particle inclusions are associated with laser induced damage formations of optics due to higher absorption and electromagnetic field enhancement. The Laserzentrum Hannover has prepared a coating with a defined concentration of gold nanoparticles within a buffer layer for investigation studies of such inclusions. Under naphthalene atmosphere was the influence of the inclusions quite strong and reduced the damage threshold in the order of one magnitude. With the variation of the fluence were different steps of contamination behavior investigated and former contamination model was confirmed. Also, the coatings with

nanoparticle inclusions were investigated with an atmosphere of high oxygen -
naphthalene ratio. The atmosphere composition improved the performance of
the optics up to high fluences of $830\,\text{mJ/cm}^2$, corresponding to an equivalent
fluence like the performed blank test, which also show no transmission loss.
All in all, the cooperational work proved the strong influence of nano-sized
inclusions as well as was the positive effect of oxygen shown.

After many successful irradiation tests under high oxygen - naphthalene ratio
is the question of a generalized oxygen effect, regarding to unknown contam-
inants. Transforming the test method to real contaminants, which are used
for the construction of satellite systems, is crucial. The investigations were
performed under a solithane atmosphere with an equivalent contamination
pressure like it was used for naphthalene tests and the optics were irradiate
under the relevant satellite fluence of $1\,\text{J/cm}^2$. Deposition of solithane was
shown within 7.2M pulses, what will result in damage formation within the
planned operational time of 36 months and a pulsenumber of more than a
billion. Consider here, that under the test parameters of $1\,\text{J/cm}^2$ and a naph-
thalene pressure of 10^{-5} mbar the optics get broken within less than 1 M pulses.
This arises the conclusion, that naphthalene is a very aggressive contaminant
regarding to laser induced contamination.The oxygen - solithane tests were
performed under the planned $40\,\text{Pa}$ oxygen pressure of the ADM Aeolus satel-
lite. An in-situ tracking of the contamination concentration was due to the
technical restriction of the RGA system not possible, but a test with the same
contamination conditions without oxygen were performed directly after the
21.6M pulses test and showed deposition phenomena. The in-situ as well ex-
situ investigation of the longterm test have not revealed a disturbance of the
surface within the irradiated area. Moreover the transmission remained very
high at 98%. The effect of the cleaning mechanism was performed also and
much of the deposited contamination was cleaned. But the investigation with
the high magnification of the scanning electron microscopy found crack forma-
tions within the deposition area. This phenomena was not exhibited at lower
fluence and naphthalene as contaminant, but the high fluence of the laser beam
increases the probability of laser damage occurrence on absorbing spots.

Consequently, it is important to insert oxygen within the satellite system from
the first moment of operation to prevent deposition as well as crack forma-
tions.

5.2   Outlook

The presented tests and results were performed under the repetition rate of
$1\,\mathrm{kHz}$. The oxygen and contaminants compete with adsorbing places on the
surface. The repetition rate leads to an adsorbing interval of $1\,\mathrm{ms}$ between
each pulse. The question arises, if a higher adsorbing interval will lead to a
high laser induce contamination.

Scanning electron microscope with its high magnification enables the investiga-
tion of single pulse phenomena regarding to the laser induced contamination.
Surface can be inspected with higher resolution and the LIC phenomena can
investigated in combination of an element analysis

Moreover, further tests with nanoparticle inclusions are planned in dependency
of the buffer layer thickness. Influence of the artificial nanoparticel can be in-
vestigated in dependence of the inclusion depths.

Additionally, a more intensive view on the chemical reaction can determine
the possible reactions of oxygen on the contamination in a more quantitative
aspect.

References

[1] ESA: *European Data Relay System (EDRS)*. Webpage (2014). *http : //esa.int/Our_Activities/Telecommunications/_Integrated_Appli − cations/EDRS*.

[2] ESA: *LISA Pathfinde Mission*. Webpage (2013). *http : //esa.int/Our_Activities/Space_Science/LISA_Pathfinder_overview*.

[3] P. Clissold: *ADM-AEOLUS: science report*. In: *ESA Special Publication*, vol. 1311 (2008).

[4] H.-J. Eichler, A. Fleischer, J. Kross, M. Krytek, H. Lang, H. Niedrig, H. Rauch, G. Schmahl, H. Schoenbeck, E. Sedlmayr *et al.*: *Bergmann, Schäfer/Lehrbuch der Experimentalphysik/Band 3—Optik*. de Gruyter, Berlin - New York (2004).

[5] B. H. Weiller, J. D. Fowler, and R. M. Villahermosa: *Inhibition of contamination laser induced damage to optical substrates*. In: *Laser Damage Symposium XLII: Annual Symposium on Optical Materials for High Power Lasers*, 784229–784229. International Society for Optics and Photonics (2010).

[6] B. H. Weiller, J. D. Fowler, and R. M. Villahermosa: *Contamination resistant coatings for enhanced laser damage thresholds*. In: *SPIE Laser Damage*, 85302A–85302A. International Society for Optics and Photonics (2012).

[7] S. Becker, A. Pereira, P. Bouchut, F. Geffraye, and C. Anglade: *Laser-induced contamination of silica coatings in vacuum*. In: *Boulder Damage Symposium XXXVIII: Annual Symposium on Optical Materials for High*

Power Lasers, 64030J–64030J. International Society for Optics and Photonics (2006).

[8] W. Riede, H. Schroeder, G. Bataviciute, D. Wernham, A. Tighe, F. Pettazzi, and J. Alves: *Laser-induced contamination on space optics*. In: *XLIII Annual Symposium on Optical Materials for High Power Lasers*, 81901E–81901E. International Society for Optics and Photonics (2011).

[9] D. Wernham, J. Alves, F. Pettazzi, and A. Tighe: *Laser-induced contamination on the ALADIN laser for ADM-Aeolus*. In: G. Exarhos, Vitaly, E. Gruzdev, J. A. Menapace, D. Ristau, and M. J. Soileau (Eds.), *Laser-Induced Damage in Optical Materials*, vol. 7842. SPIE (2010).

[10] T. H. Mainman: *Stimulated Optical Radiation in Ruby*. Nature **187**, 493–494 (1960).

[11] S. Martin: *Zerstörmechanismen in optischen Materialien bei Anregung mit ultrakurzen Laserpulsen*. Ph.D. thesis, Freie Universität Berlin, Germany (2005).

[12] H. Fischer and H. Kaul: *Mathematik für Physiker - Band 1: Grundkurs*. B. G. Teuber Verlag, Stuttgart - Leipzig - Wiesbaden (2005).

[13] D. Ristau: *Laser-Induced Damage in Optical Materials*. CRC Press (2014).

[14] N. W. Ashcroft and D. N. Mermin: *Festkörperphysik*. Oldenbourg Verlag (2005).

[15] R. Hopper and D. R. Uhlmann: *Mechanism of inclusion damage in laser glass*. Journal of Applied Physics **41**, 4023–4037 (1970).

[16] M. F. Koldunov, A. A. Manenkov, and I. L. Pokotilo: *Formulation of the criterion of thermoelastic laser damage of transparent dielectrics and the dependence of the damage threshold on the pulse duration*. Quantum Electronics **27**, 918–922 (1997).

[17] M. F. Koldunov, A. A. Manenkov, and I. L. Pokotilo: *Mechanical damage in transparent solids caused by laser pulses of different durations*. Quantum electronics **32**, 335 (2002).

[18] S. Papernov and A. Schmid: *Correlations between embedded single gold*

nanoparticles in SiO2 thin film and nanoscale crater formation induced by pulsed-laser radiation. Journal of Applied Physics **92**, 5720–5728 (2002).

[19] C. Carr, H. Radousky, A. Rubenchik, M. Feit, and S. Demos: *Localized dynamics during laser-induced damage in optical materials.* Physical review letters **92**, 087401 (2004).

[20] S. Papernov and A. Schmid: *Localized absorption effects during 351 nm, pulsed laser irradiation of dielectric multilayer thin films.* Journal of applied physics **82**, 5422–5432 (1997).

[21] P. Grua, J. Morreeuw, H. Bercegol, G. Jonusauskas, and F. Vallée: *Electron kinetics and emission for metal nanoparticles exposed to intense laser pulses.* Physical Review B **68**, 035424 (2003).

[22] K. Saito and A. Ikushima: *Absorption edge in silica glass.* Physical Review B **62**, 8584 (2000).

[23] J. Bude, G. Guss, M. Matthews, and M. Spaeth: *The effect of lattice temperature on surface damage in fused silica optics.* In: *Boulder Damage Symposium XXXIX: Annual Symposium on Optical Materials for High Power Lasers*, 672009–672009. International Society for Optics and Photonics (2007).

[24] C. Duthler: *Explanation of laser-damage cone-shaped surface pits.* Applied Physics Letters **24**, 5–7 (1974).

[25] N. Bloembergen: *Role of cracks, pores, and absorbing inclusions on laser induced damage threshold at surfaces of transparent dielectrics.* Applied Optics **12**, 661–664 (1973).

[26] S. Foltyn: *Spotsize effects in laser damage testing.* NBS Spec. Publ **669**, 368 (1984).

[27] A. P. Tighe, F. Pettazzi, J. Alves, D. Wernham, W. Riede, H. Schroeder, P. Allenspacher, and H. Kheyrandish: *Growth mechanisms for laser induced contamination on space optics in vacuum.* In: *Boulder Damage Symposium XL Annual Symposium on Optical Materials for High Power Lasers*, 71321L–71321L. International Society for Optics and Photonics (2008).

[28] H. Schröder, P. Wagner, D. Kokkinos, W. Riede, and A. Tighe: *Laser-induced contamination and its impact on laser damage threshold.* In: *SPIE Laser Damage*, 88850R–88850R. International Society for Optics and Photonics (2013).

[29] P. H. Krupenie: *The spectrum of molecular oxygen.* Journal of physical and chemical reference data **1**, 423–534 (1972).

[30] J. Poveda, A. Guerrero, I. Álvarez, and C. Cisneros: *Multiphoton ionization and dissociation of naphthalene at 266, 355, and 532nm.* Journal of Photochemistry and Photobiology A: Chemistry **215**, 140–146 (2010).

[31] NASA: *Hubble Servicing Missions Overview.* Webpage (2015). *www.nasa.gov/mission_pages/hubble/servicing/index.html.*

[32] P. Baumeister: *Optical coating technology*, vol. 137. SPIE Press Bellingham (2004).

[33] J. Ebert and M. Ebert: *Magnetron-Sputtern im Mikrowellenplasma im Vergleich zu konventionellen Aufdampfverfahren.* PHOTONIK **34**, 34–39 (2002).

[34] J. Grooves, H. Wadley, A. Ritenour, D. Hass, and P. Ratnaparkhi: *Electron Beam Directed Vapor Deposition.* Proceeding, Electron Beam Melting and Refining State of the Art (1997).

[35] H. Ehlers, M. Lappschies, N. Beermann, and D. Ristau: *Neue optische Beschichtungen.* Optik & Photonik **2**, 41–46 (2007).

[36] A. Gorshkov, I. Bel'bas, M. Maslov, V. Sannikov, and K. Vukolov: *Laser damage investigations of Cu mirrors.* Fusion engineering and design **74**, 859–863 (2005).

[37] J. F. W. Herschel: *'Αμορ$\Phi\omega\tau\alpha$ No. I. On a Case of Superficial Colour Presented by a Homogeneous Liquid Internally Colourless.* Philosophical Transactions of the Royal Society of London 143–145 (1845).

[38] J. R. Lakowicz: *Principles of fluorescence spectroscopy.* Springer Science & Business Media (2007).

[39] I. Berlman: *Handbook of florescence spectra of aromatic molecules.* Academic Press, New York (1971).

[40] G. G. Stokes: *On the change of refrangibility of light.* Philosophical Transactions of the Royal Society of London 463–562 (1852).

[41] M. Kasha: *Characterization of electronic transitions in complex molecules.* Discuss. Faraday Soc. **9**, 14–19 (1950).

[42] I. B. H. Schröder, G. Bataviciute: *Optical components materials and process development and validation for high power space borne lasers (Phase I Report)* (2003).

[43] H. H. Telle, A. G. Ureņa, and R. J. Donovan: *Laser chemistry: spectroscopy, dynamics and applications.* John Wiley & Sons (2007).

[44] D. Kuhn: *Messung von Temperatur-und Konzentrationsprofilen mittels laserinduzierter Fluoreszenz (LIF).* Ph.D. thesis (2001).

[45] M. Peleg, M. G. Corradini, and M. D. Normand: *Kinetic models of complex biochemical reactions and biological processes.* Chemie Ingenieur Technik **76**, 413–423 (2004).

[46] M. E. Turner, E. L. Bradley, K. A. Kirk, and K. M. Pruitt: *A theory of growth.* Mathematical Biosciences **29**, 367–373 (1976).

[47] S. H. Strogatz: *Nonlinear dynamics and chaos: with applications to physics, biology, chemistry, and engineering.* Westview press (2014).

[48] D. N. Chatterjee: *Electron Microprobe Analysis.* Course 12.141 (2012).

[49] I. Balasa, M. Hippler, H. Schröder, L. Jensen, M. Gauch, D. Ristau, and W. Riede: *Enhancement of contamination growth and damage by absorption centers under UV irradiation.* In: *SPIE Laser Damage*, 92372A. International Society for Optics and Photonics (2014).

[50] W. Riede, P. Allenspacher, M. Lammers, D. Wernham, A. Ciapponi, C. Heese, L. Jensen, H. Maedebach, S. Schrameyer, and D. Ristau: *From ground to space: How to increase the confidence level in your flight optics.* In: *SPIE Laser Damage*, 88850D–88850D. International Society for Optics and Photonics (2013).

[51] ESA: *A.10.1 Araldite.* Webpage. *http : //esmat.esa.int/a10_1.htm.*

[52] ESA: *A.14.10 Solithane.* Webpage. *http : //esmat.esa.int/a14_10.htm.*

List of Figures

List of Tables

Appendix

Static contamination series

Description: In the following tables are listed all relevant experiments for the stationary measurement procedure of this thesis.
The appreviations RO, LO and LU describe the position of the sample during the experiment.

Test-Nr	Fluence [J/cm^2] $\pm\,10\,\%$	Duration [min]	P_{C} [mbar] $\pm\,10\,\%$	P_{Oxygen} [Pa] $\pm\,10\,\%$
Test06	1200	60	$4 \cdot 10^{-5}$	10
Test07	1200	60	$4 \cdot 10^{-5}$	1
Test08	1200	60	$4 \cdot 10^{-5}$	40

Table 0.1: Sample-Series 1015 with Sample 1015 (MS) - RO, 1068 (e-beam) - LO, 1139 (uncoated silica) - LU

Test-Nr	Fluence [J/cm²] ± 10 %	Duration [min]	P_C [mbar] ± 10 %	P_{Oxygen} [Pa] ± 10 %
Test00	66	60	$1.1 \cdot 10^{-5}$	0
Test01	100	60	$1.1 \cdot 10^{-5}$	0
Test02	280	60	$4 \cdot 10^{-5}$	40
Test03	270	60	$4 \cdot 10^{-5}$	10
Test04	270	60	$4 \cdot 10^{-5}$	1
Test05	270	60	$4 \cdot 10^{-5}$	0.05
Test06	270	60	$4 \cdot 10^{-5}$	0
Test07	300	60	0	0
Test08	605	60	$4 \cdot 10^{-5}$	0
Test09	590	60	$4 \cdot 10^{-5}$	40
Test10	585	60	$4 \cdot 10^{-5}$	10
Test11	570	60	$4 \cdot 10^{-5}$	1

Table 0.2: Sample-Series 1017 with Sample 1017 (MS) - RO, 1038 (e-beam) - LO, 1141 (uncoated silica) - LU

Test-Nr	Fluence [J/cm²] ± 10 %	Duration [min]	P_C [mbar] ± 10 %	P_{Oxygen} [Pa] ± 10 %
Test00	640	60	0	0
Test01	920	60	0	0
Test02	880	60	$4 \cdot 10^{-5}$	40
Test03	860	60	$4 \cdot 10^{-5}$	0
Test04	970	60	$4 \cdot 10^{-5}$	10
Test05	900	60	$4 \cdot 10^{-5}$	1
Test06	870	60	$8 \cdot 10^{-5}$	40
Test07	850	60	$8 \cdot 10^{-5}$	10
Test08	850	60	$8 \cdot 10^{-5}$	1
Test10	600	10	$4 \cdot 10^{-5}$	10
Test11	600	15	$4 \cdot 10^{-5}$	10

Table 0.3: Sample-Series 1041 with Sample 1041 (e-beam) - RO, 1018 (MS) - LO, 1142 (uncoated silica) - LU

Test-Nr	Fluence [J/cm^2] $\pm\,10\,\%$	Duration [min]	P_C [mbar] $\pm\,10\,\%$	P_Oxygen [Pa] $\pm\,10\,\%$
Test00	680	60	$8\cdot10^{-5}$	40
Test01	640	60	$8\cdot10^{-5}$	10
Test02	620	60	$8\cdot10^{-5}$	1
Test03	610	60	$8\cdot10^{-5}$	0
Test04	300	60	$8\cdot10^{-5}$	40
Test05	300	60	$8\cdot10^{-5}$	10
Test06	300	60	$8\cdot10^{-5}$	1
Test07	270	60	$8\cdot10^{-5}$	0
Test08	350	60	$8\cdot10^{-5}$	1
Test09	650	60	$8\cdot10^{-5}$	40

Table 0.4: Sample-Series 1019 with Sample 1019 (MS) - RO, 1042 (e-beam) - LO, 1143 (uncoated silica) - LU

Dynamic contamination series

Description: In the following tables are listed all relevant experiments for the dynamic measurement procedure of this thesis.

The appreviations RO, LO and LU describe the position of the sample during the experiment.

Test-Nr	Fluence [J/cm^2] $\pm$ 10 %	Duration [min]	P_{C} [mbar] $\pm$ 10 %	ratio $P_{O_2} : P_{\mathrm{C}}$ $\pm$ 10 %
Test03	860	60	$1 \cdot 10^{-4}$	1000:1
Test04	820	60	$1.5 \cdot 10^{-5}$	0:1
Test08	850	60	$1 \cdot 10^{-4}$	100:1

Table 0.5: Sample-Series 1020 with Sample 1020 (MS) - RO, 1215 (e-beam) - LO, 1144 (uncoated silica) - LU

Test-Nr	Fluence [J/cm^2] $\pm 10\%$	Duration [min]	P_C [mbar] $\pm 10\%$	ratio $P_{O_2} : P_C$ $\pm 10\%$
Test01	960	60	0	0
Test02	900	60	$1 \cdot 10^{-4}$	10:1
Test04	900	60	$1 \cdot 10^{-4}$	50:1
Test05	890	60	$1 \cdot 10^{-4}$	4000:1
Test06	550	60	$1 \cdot 10^{-4}$	10:1
Test07	550	60	$1 \cdot 10^{-4}$	50:1
Test08	580	60	$1 \cdot 10^{-4}$	100:1
Test09	570	60	$1 \cdot 10^{-4}$	1000:1

Table 0.6: Sample-Series 1021 with Sample 1021 (MS) - RO, 1216 (e-beam) - LO, 1173 (uncoated silica) - LU

Test-Nr	Fluence [J/cm^2] $\pm 10\%$	Duration [min]	P_C [mbar] $\pm 10\%$	ratio $P_{O_2} : P_C$ $\pm 10\%$
Test01	590	60	$1 \cdot 10^{-4}$	4000:1
Test02	310	60	$1 \cdot 10^{-4}$	10:1
Test03	300	60	$1 \cdot 10^{-4}$	50:1
Test04	310	60	$1 \cdot 10^{-4}$	100:1
Test05	310	60	$1 \cdot 10^{-4}$	1000:1
Test06	310	60	$1 \cdot 10^{-4}$	4000:1
Test07	310	60	$1 \cdot 10^{-5}$	10:1
Test08	310	60	$1 \cdot 10^{-5}$	50:1

Table 0.7: Sample-Series 1022 with Sample 1022 (MS) - RO, 1217 (e-beam) - LO, 1174 (uncoated silica) - LU

Test-Nr	Fluence [J/cm²] ± 10 %	Duration [min]	P_C [mbar] ± 10 %	ratio $P_{O_2} : P_C$ ± 10 %
Test00	300	10	$1.4 \cdot 10^{-5}$	0:1
Test01	300	10	$1.4 \cdot 10^{-5}$	40 Pa cleaning
Test02	300	14	$1.4 \cdot 10^{-5}$	0:1
Test03	300	14	$1.4 \cdot 10^{-5}$	40 Pa cleaning
Test04	200	25	$1.4 \cdot 10^{-5}$	0:1
Test05	200	25	$1.4 \cdot 10^{-5}$	40 Pa cleaning
Test06	150	60	$1.4 \cdot 10^{-5}$	0:1
Test07	150	60	$1.4 \cdot 10^{-5}$	40 Pa cleaning
Test08	310	60	$1 \cdot 10^{-5}$	100:1
Test09	310	60	$1 \cdot 10^{-5}$	1000:1
Test10	310	60	$1 \cdot 10^{-5}$	4000:1
Test11	620	60	$1 \cdot 10^{-5}$	1000:1

Table 0.8: Sample-Series 1267 with Sample 1267 (MS) - RO, 1218 (e-beam) - LO, 1175 (uncoated silica) - LU

Test-Nr	Fluence [J/cm²] ± 10 %	Duration [min]	P_C [mbar] ± 10 %	ratio $P_{O_2} : P_C$ ± 10 %
Test00	600	60	$1 \cdot 10^{-5}$	100:1
Test01	600	60	$1 \cdot 10^{-5}$	10:1
Test02	600	60	$1 \cdot 10^{-5}$	50:1
Test03	600	60	$1 \cdot 10^{-5}$	4000:1
Test04	900	60	$1 \cdot 10^{-5}$	4000:1
Test05	900	60	$1 \cdot 10^{-5}$	1000:1
Test06	850	60	$1 \cdot 10^{-5}$	100
Test10	850	60	$1 \cdot 10^{-5}$	50:1
Test11	600	60	$1 \cdot 10^{-5}$	10:1

Table 0.9: Sample-Series 1268 with Sample 1268 (MS) - RO, 1176 (uncoated silica) - LO, 1219 (e-beam) - LU

Test-Nr	Fluence [J/cm^2] $\pm\,10\,\%$	Duration [min]	P_{C} [mbar] $\pm\,10\,\%$	ratio $P_{O_2}:P_{\mathrm{C}}$ $\pm\,10\,\%$
Test00	900	360	$1 \cdot 10^{-5}$	4000:1
Test01	1000	60	$1 \cdot 10^{-5}$	10:1
Test02	900	360	$1 \cdot 10^{-5}$	4000:1
Test03	900	360	$1 \cdot 10^{-4}$	4000:1
Test04	900	60	$1 \cdot 10^{-5}$	4000:1
Test05	900	60	$1 \cdot 10^{-5}$	10000:1
Test06	100	120	$1 \cdot 10^{-5}$	LIC-Cleaning sequence
Test07	100	7	$1 \cdot 10^{-5}$	LIC-Deposition
Test08	1000	60	$1 \cdot 10^{-5}$	0:1
Test09	900	60	$1 \cdot 10^{-5}$	0:1
Test10	900	60	$1 \cdot 10^{-5}$	0:1

***Table 0.10:*** Sample-Series 1269 with Sample 1269 (MS) - RO, 1220 (e-beam) - LO, 1271 (IBS) - LU

Test-Nr	Fluence [J/cm^2] $\pm\,10\,\%$	Duration [min]	P_{C} [mbar] $\pm\,10\,\%$	ratio $P_{O_2}:P_{\mathrm{C}}$ $\pm\,10\,\%$
Test00	1100	90	$1 \cdot 10^{-5}$	Deposition
Test01	1200	60	$1 \cdot 10^{-5}$	Deposition
Test02	1100	60	$1 \cdot 10^{-5}$	blank test
Test03	1100	120	$1 \cdot 10^{-4}$	Deposition
Test04	1100	120	$1 \cdot 10^{-5}$	10000:1
Test05	1100	120	$1 \cdot 10^{-5}$	1000:1
Test06	1100	120	$1 \cdot 10^{-5}$	> 1000:1
Test07	1100	240	$1 \cdot 10^{-5}$	LIC-Cleaning
Test08	1000	360	$1 \cdot 10^{-5}$	> 10000:1
Test09	1100	60	$1 \cdot 10^{-5}$	0:1

Table 0.11: Sample-Series 1270 with Sample 1270 (MS) - RO, 1221 (e-beam) - LO, 1272 (IBS) - LU. Experimental series with spaceborne contaminants: Test00 and Test01 with araldite, the Test03 - Test09 with solithane
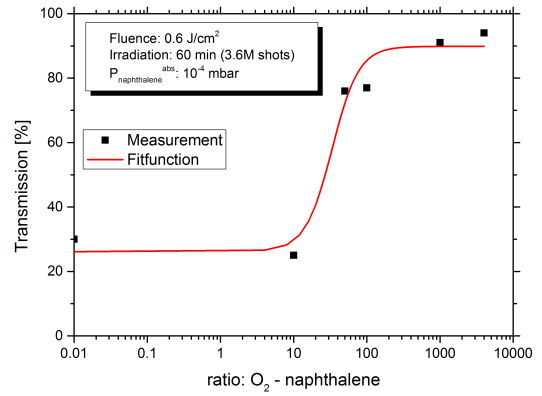
Fitfunction of the experimental series

The following graphs illustrate the fitfunctions of the growth model corresponding to the measured transmission values over an irradiation of $3.6\,M$ pulses for various measurement parameter.
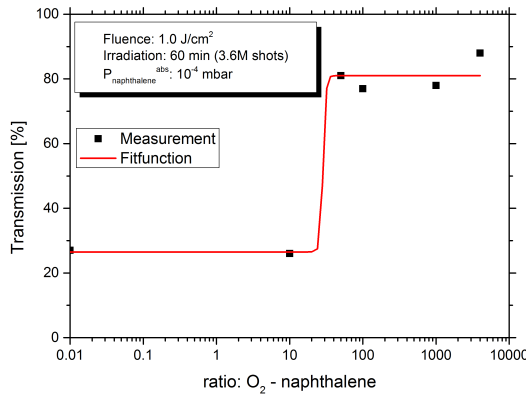
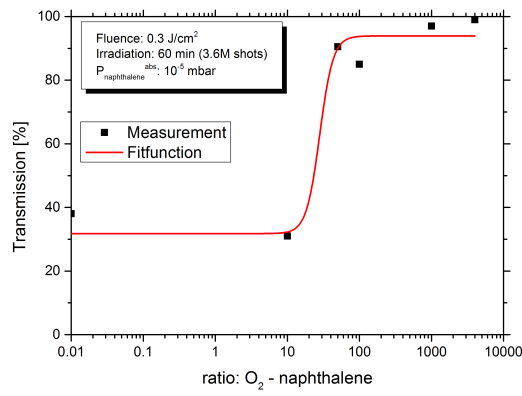**e-beam with abs. naphthalene pressure $10^{-4}\,$mbar**
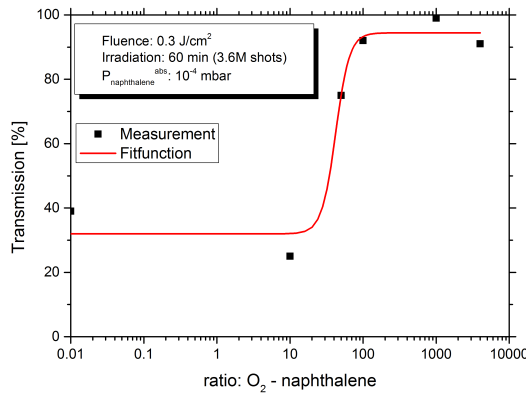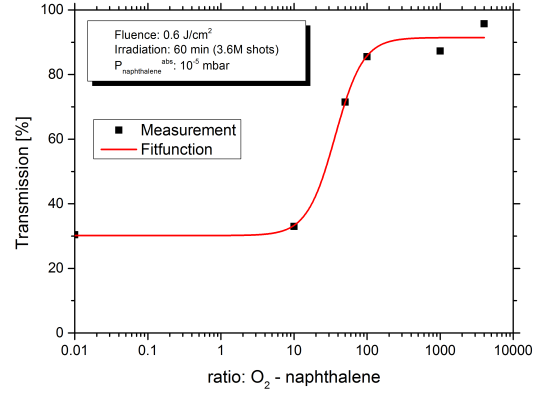

(a) low fluence

(b) medial fluence

(c) high fluence

Figure 0.1: Transmission values over the contamination ratio of e-beam AR coating for an absolute naphthalene pressure of $10^{-4}\,$mbar and the corresponding fitfunction
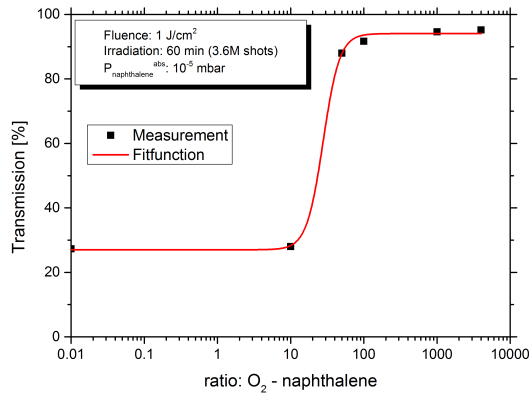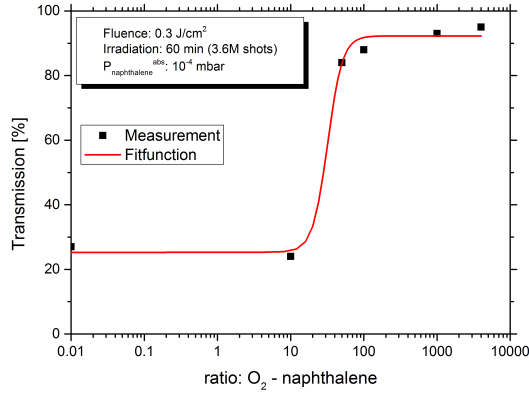
e-beam with abs. naphthalene pressure 10^{-5} mbar

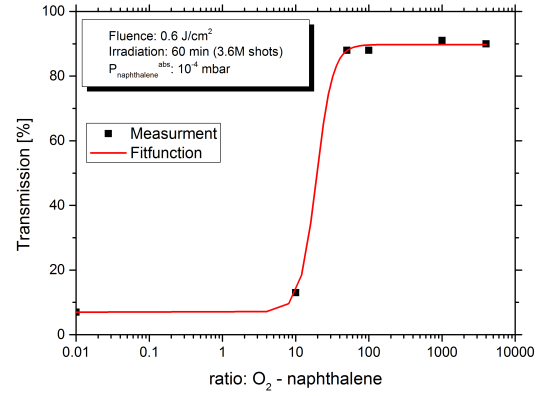
(a) low fluence

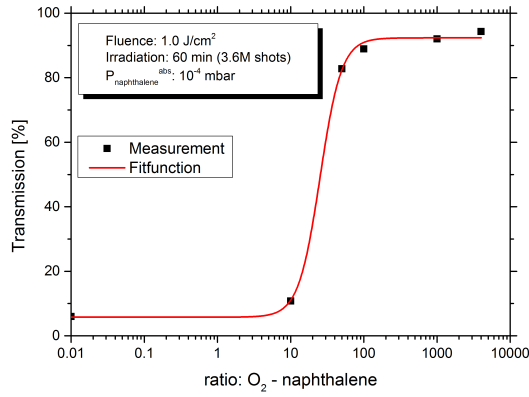(b) medial fluence

(c) high fluence

Figure 0.2: Transmission values over the contamination ratio of e-beam AR coating for an absolute naphthalene pressure of 10^{-5} mbar and the corresponding fitfunction

MS with abs. naphthalene pressure 10^{-4} mbar

(a) low fluence

(b) medial fluence

(c) high fluence

Figure 0.3: Transmission values over the contamination ratio of MS AR coating for an absolute naphthalene pressure of 10^{-4} mbar and the corresponding fitfunction

MS with abs. naphthalene pressure 10^{-5} mbar

(a) low fluence

(b) medial fluence

(c) high fluence

Figure 0.4: Transmission values over the contamination ratio of MS AR coating for an absolute naphthalene pressure of 10^{-5} mbar and the corresponding fitfunction
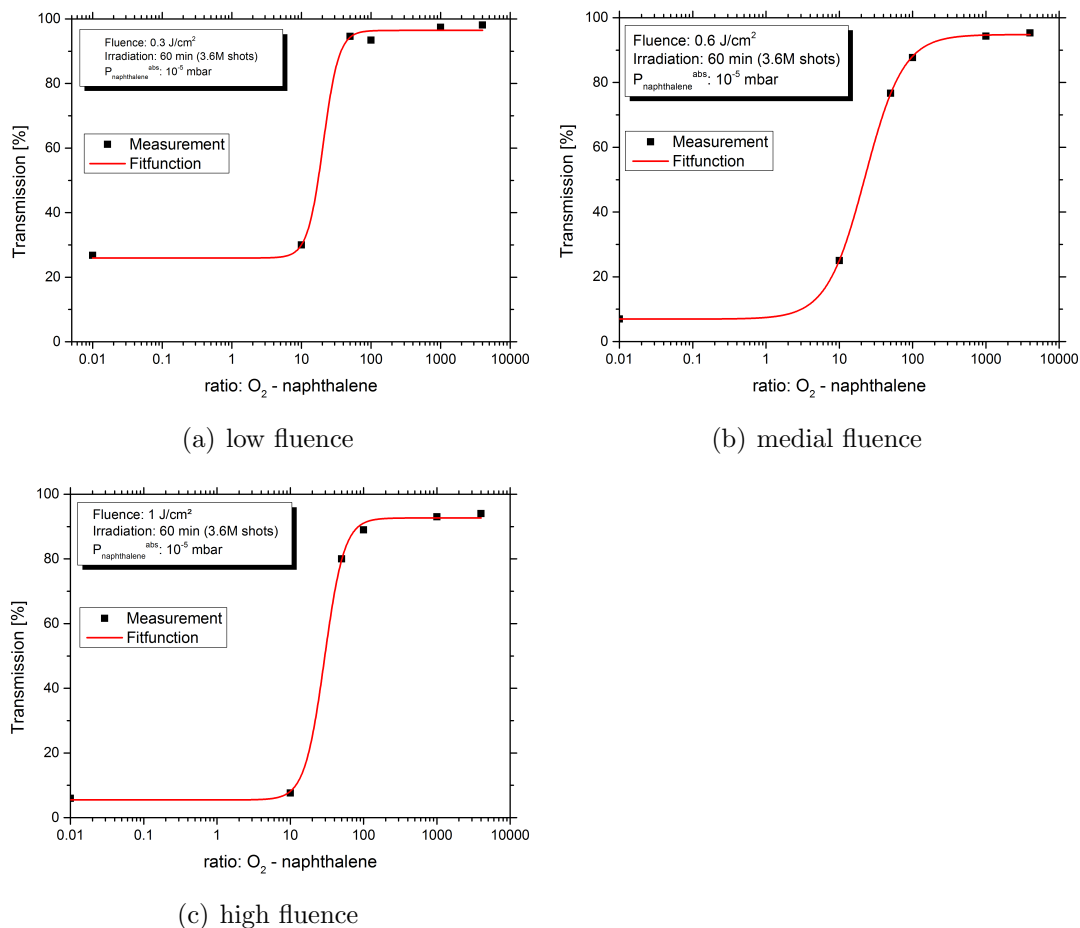
Eidesstaatliche Erklärung

Hiermit erkläre ich, Markus Hippler, geboren am 21. April 1990 in Torgau, dass ich die vorliegende Diplomarbeit mit dem Titel: "Influence of Oxygen on laser induced Contamination" selbstständig und ohne unzulässiger Hilfe Dritter angefertigt habe. Alle verwendeten Quellen und sinngemäßen Zitate wurden kenntlich gemacht und entsprechend im Quellenverzeichnis angegeben.

<div align="right">

Markus Hippler

Dresden, den 20. Mai 2015

</div>